Application of Zernike Phase Plate to Transmission Electron Microscopy

A thesis presented to the faculty of

Department of Physiological Science, School of Life Science,

The Graduate University for Advanced Studies

in partial fulfillment of the requirements

for the degree of Doctor of Philosophy

by

Radostin Danev

August 27, 2001

The Graduate University for Advanced Studies

Okazaki, Japan

Table of contents

Abstract.

Abstract

The possibility of implementing a Zernike phase plate in a transmission electron microscope is investigated both theoretically and experimentally. The phase-retarding plate in the form of thin film with a hole in the center is positioned in the back-focal plane of the objective lens. The experiments showed that the phase plate functions as predicted, producing a cosine-type phase contrast transfer function. Images of negatively stained horse spleen ferritin were highly improved in the contrast and the image-modulation, compared to those acquired without the phase plate. Electrostatic charging and related difficulties were encountered during the phase plate experiments.

The radial distribution of the beam-induced charge in thin films was investigated using the contrast transfer properties of the transmission electron microscope. The phase shift due to charging was measured as the phase difference between the contrast transfer functions of two photos taken with and without film at the back focal plane. Solving the inverse Laplace problem with this input data recovers the charge density of the measured film. The surface charge density reaches quasi-equilibrium state after the first 30 min of the electron beam pre-irradiation. An explanation of the qualitative behavior of the charge density, based on the contamination diffusion theory, is proposed.

The first experimental realization of the complex reconstruction scheme is presented. Two images taken with and without Zernike phase plate are used for the extraction of both the phase and the amplitude of the object wave. New "off-plane" application scheme for the phase plate was developed, to overcome various practical problems. Aberration-corrected phase images of negatively stained horse spleen ferritin and tobacco mosaic virus samples are free from image distortion and show extraordinary high contrast compared to that obtained with conventional TEM.

1. PHASE TRANSMISSION ELECTRON MICROSCOPE – A NEW TOOL FOR HIGH EFFICIENCY BIOLOGICAL OBSERVATIONS

The phase contrast mechanism plays a major role in the high resolution observation of biological samples with transmission electron microscope (TEM). Such samples are composed mainly of low atomic number elements which makes them essentially transparent to high-energy electrons. The application of higher accelerating voltages and techniques such as ice embedding worsens the contrast problem even further.

Currently, the phase contrast in TEM is realized through defocusing of the objective lens. As a result only part of the spatial frequency components in the object exit wave are expressed in the image [1]. Particularly, the low spatial frequency components, which are vital in biological observations (low frequency object information, particle finding, image alignment), are severely suppressed. Currently, there is no practical solution for this problem of loss of information. The most common remedy is to take defocus series of the object, followed by a numerical reconstruction of the object phase [2,3]. This approach requires that several photos be taken from the same sample area thus increases the possibility of radiation damage. Another approach is the use of energy filtering. By removing the inelastic contributions to the images, a higher contrast and a better signal-to-noise ratio can be reached for the low frequency components [4]. The effect is due to reduction of the background noise. However, a loss of signal still exists as the phase contrast transfer is not affected.

In light microscopy, the phase observation problem has been solved about 60 years ago by Zernike [5]. The implementation of a phase plate positioned in the diffraction plane leads to a pure phase imaging. There have been several attempts to apply this technique to TEM [6-12]. Most of these showed promising results, however, due to various practical problems such as charging, contamination, difficulties in positioning and a too demanding fabrication, none

1

remains in use. Another promising idea is Boersch's electrostatic phase plate which has not yet been realized in practice [13].

This Chapter describes our experimental trial on the application of a Zernike-type phase plate to TEM. The Chapter is organized as follows. In section 1.1. is described the basic image formation theory of TEM followed by a discussion of the observation restrictions in the conventional TEM (CTEM). In section 1.2. the theory behind the application of Zernike-type phase plate in TEM is presented. Materials for phase plate preparation and image formation theory are discussed. Section 1.3. contains experimental procedures and representative results from our trial on the application of Zernike phase plate. The section concludes with a discussion of the results.

1.1. Image formation theory and observation limitations in TEM.

1.1.1. Deviations from the perfect optical system.

The TEM being an optical system shares most of the problems observed in the light optical systems. In Fig.1 are illustrated ideal (Fig.1a) and practical (Fig.1b) optical systems. In the ideal system the spherical wave emerged from a point object, positioned at the front-focal plane of the objective, is converted to plane wave at the back-focal plane of the lens (Fraunhofer diffraction) [14 p.425]. Practical systems however suffer various imperfections (defocus, spherical aberration, chromatic aberration, coma, astigmatism, and other [15 p.31-40]) resulting in a non-planar wavefront at the back-focal plane of the objective. The combined effect of the various imperfections could be described as additional phase shift exerted on the wave at the back-focal plane (Fig.1b) [15 p.71]. For the purpose of out investigation we will restrict the consideration to defocus and spherical aberration of the objective lens as the other imperfections are either optically correctable [15 p.40] or their effect on the image is insignificant [15 p.32].

1.1.2. Image Formation in TEM.

For description of the image formation in TEM usually the so-called Contrast Transfer Function (CTF) formalism is used. The method was first developed in light microscopy and subsequently applied to TEM by Hanszen [16,17]. The wave immediately after the object (object wave) is first propagated to the back-focal plane through an ideal objective lens (free from any aberrations) by a Fourier transform. The resulting diffraction pattern is then modulated by the Contrast Transfer Function (CTF) which includes all the effects due to various imperfections of the optical system. Subsequent Fourier transform gives the wave at the image plane. The image will be the square of the modulus of the object wave as the intensity is the observable quantity.

In Fig.2 is illustrated the image formation modeling mechanism. Let us consider an object wave in the form:

$$\psi(\vec{r}) = A(\vec{r}) e^{i\Phi(\vec{r})}, \tag{1.1}$$

where $A(\vec{r})$ is the amplitude and $\Phi(\vec{r})$ is the phase of the wave. Propagation to the back-focal plane of the objective lens is performed through a Fourier transform giving:

$$\Psi(\vec{k}) = \mathrm{FT}\{\psi(\vec{r})\} = \mathrm{FT}\{A(\vec{r})e^{i\Phi(\vec{r})}\}, \tag{1.2}$$

where FT{ } denotes Fourier transform, $\vec{k}$ is the spatial frequency vector. The CTF is usually written in the form:

$$G(\vec{k}) = e^{i\gamma(\vec{k})}, \tag{1.3}$$

where $\vec{k}$ is the spatial frequency vector, $\gamma(\vec{k})$ is a phase shift function:

$$\gamma(\vec{k}) = 2\pi \left(-\frac{1}{2} \lambda \, \Delta z \, k^2 + \frac{1}{4} \lambda^3 \, C_s \, k^4 \right), \tag{1.4}$$

where C_S is the spherical aberration coefficient of the objective lens, Δz is the defocus value, λ is the electron wavelength. The phase shift depends only on the modulus of the spatial frequency vector k as only axially symmetric distortions are considered. The notations underfocus for $\Delta z > 0$ (specimen below the front-

3

focal plane of the objective) and overfocus for $\Delta z < 0$ (specimen above the focal plane) will be used.

Modulation of the diffraction wave (Eq. 1.2) by the CTF (Eq. 1.3) produces the modulated diffraction wave:

$$\Psi'(\vec{k}) = \Psi(\vec{k})\,G(\vec{k}) = FT\{A(\vec{r})e^{i\Phi(\vec{r})}\}e^{i\gamma(\vec{k})}.\tag{1.5}$$

The Fourier transform of the modulated diffraction wave gives the image wave:

$$\psi_i(\vec{r}) = FT\{\Psi'(\vec{k})\} = FT\{FT\{A(\vec{r})e^{i\Phi(\vec{r})}\}e^{i\gamma(\vec{k})}\}.\tag{1.6}$$

The image intensity will be the square of the modulus of the image wave:

$$I(\vec{r}) = |\psi_i(\vec{r})|^2 = \psi_i(\vec{r})\,\psi_i^*(\vec{r}).\tag{1.7}$$

The formalism described above does not provide a clear picture of how exactly the amplitude and the phase of the object wave are represented in the image. With appropriate approximations however it is possible to separate the amplitude and the phase transfer mechanisms.

1.1.3. Weak object approximation.

Biological specimens (macromolecules, viruses etc.) observed by TEM are relatively thin making them almost transparent for the high-energy electrons. Thus the disturbances to the amplitude and the phase of the incident wave are small. Assuming that $A(\vec{r})$ is close to unity and $\Phi(\vec{r})$ is close to zero we can write an approximate form of the object wave (from Eq. 1.1):

$$\psi(\vec{r}) = (1 + a(\vec{r}))\,e^{i\Phi(\vec{r})} \approx (1 + a(\vec{r}))(1 + i\Phi(\vec{r})) \approx 1 + a(\vec{r}) + i\Phi(\vec{r}),\tag{1.8}$$

where $a(\vec{r}) = A(\vec{r}) - 1$ is a small disturbance to the incident wave amplitude. Eq. 1.5 then could be rewritten as:

$$\Psi'(\vec{k}) = FT\{1 + a(\vec{r}) + i\Phi(\vec{r})\}e^{i\gamma(\vec{k})} = \delta(0) + [\tilde{a}(\vec{k}) + i\tilde{\Phi}(\vec{k})]e^{i\gamma(\vec{k})},\tag{1.9}$$

where $\delta(0)$ is the Dirac delta function at zero spatial frequency, $\tilde{a}(\vec{k})$ and $\tilde{\Phi}(\vec{k})$ are the Fourier transforms of the amplitude and phase disturbances. The delta function in the above equation, also called zeroth-diffraction beam, represents the

electrons which have not been scattered by the specimen. The other term represents the object information carried by electrons scattered from the specimen. The intensity of the zeroth-diffraction beam is much higher than the intensity of the scattered beams because only a small part of the incident electrons are scattered (usually about 10 to 20 percent).

In weak object approximation Eq. 1.6 becomes (from Eq. 1.9):

$$\psi_i(\vec{r}) = FT\{\Psi'(\vec{k})\} = 1 + FT\{[\tilde{a}(\vec{k}) + i\tilde{\Phi}(\vec{k})]e^{i\gamma(\vec{k})}\} = 1 + \eta(\vec{r}) \tag{1.10}$$

here:

$$\eta(\vec{r}) = FT\{[\tilde{a}(\vec{k}) + i\tilde{\Phi}(\vec{k})]e^{i\gamma(\vec{k})}\} \tag{1.11}$$

represents the small disturbance added to the background wave (unity). The image intensity is then simplified to (from Eq. 1.7):

$$I(\vec{r}) = \psi_i(\vec{r})\,\psi_i^*(\vec{r}) = [1 + \eta(\vec{r})][1 + \eta^*(\vec{r})] = 1 + 2\,\mathrm{Re}[\eta(\vec{r})] + |\eta(\vec{r})|^2 \approx$$
$$\approx 1 + 2\,\mathrm{Re}[\eta(\vec{r})] \tag{1.12}$$

The squared term in the above equation could be neglected because of the weak object approximation. Substitution of Eq. 1.11 in Eq. 1.12 gives:

$$I(\vec{r}) = 1 + 2\,\mathrm{Re}\left[FT\{[\tilde{a}(\vec{k}) + i\tilde{\Phi}(\vec{k})]e^{i\gamma(\vec{k})}\}\right] =$$
$$= 1 + 2\,\mathrm{Re}\left[FT\{[\tilde{a}(\vec{k}) + i\tilde{\Phi}(\vec{k})][\cos(\gamma(\vec{k})) + i\sin(\gamma(\vec{k}))]\}\right] \tag{1.13}$$

By using Fourier transform properties for even, odd, real and imaginary functions it can be shown that Eq. 1.13 reduces to:

$$I(\vec{r}) = 1 + 2\,FT\{\tilde{a}(\vec{k})\cos(\gamma(\vec{k})) - \tilde{\Phi}(\vec{k})\sin(\gamma(\vec{k}))\} \ . \tag{1.14}$$

The above equation clearly illustrates the contrast transfer properties for the amplitude and phase components of the object wave. The cosine function modulating the amplitude becomes the amplitude CTF and the sine becomes the phase CTF. These contrast transfer properties of the TEM give the advantage of possibility to observe the phase of the object wave. However the microscope inherent CTFs limit the observation efficiency i.e. the information retrieved with one photo as developed in the next section.

1.1.4. Observation limitations in the CTEM.

Biological samples are composed mainly of low atomic number elements and are relatively thin making them essentially transparent for the high-energy electrons. Thus the phase of the object wave carries the majority of the information about the sample. This leads to the conclusion that the phase contrast transfer properties of the microscope are of principal importance for the biological observations.

In Fig.3a are shown representative plots of the radial component of the phase CTF ($-\sin(\gamma(k))$) as a function of the modulus of the spatial frequency vector k. The curves are calculated for acceleration voltage of 300 kV, spherical aberration coefficient C_S = 3 mm and different defocus values. From the graph it is seen that the CTF is an oscillating function with multiple zero crossings. The oscillation becomes more rapid for higher spatial frequencies. At each zero crossing the information corresponding to the given spatial frequency is lost. Around the crossings the information is severely attenuated.

For biological samples most of the information is in the characteristic size range between 1 nm and 50 nm (spatial frequency between 1 nm^{-1} and 0.02 nm^{-1}) emphasizing the contrast transfer for the lower part of the spectrum. At just focus (Fig.3a, solid line, $\Delta z = 0\,\mathrm{nm}$) the lower part of the spectrum is severely suppressed making this condition most inappropriate for biological observations. Higher defocus (Fig.3a, dotted line, $\Delta z = 615\,\mathrm{nm}$) improves the transfer for the low frequencies but also moves the first zero crossing (cutoff frequency), which limits the direct resolution of the image. By direct resolution is meant the frequency to which the image could be interpreted without additional processing. After the first zero the CTF starts to oscillate which combined with effects like partial temporal and spatial coherency of the illumination [15 p.231] dampens the transfer function (not illustrated in the figure). The combination of all these effects poses a compromise between contrast (low frequency transfer) and direct resolution (first CTF zero intercept). The increase of the defocus will provide

higher contrast but at the same time will lower the resolution. This compromise situation is a major limitation of the currently utilized TEMs. The most common remedy is to take defocus series for one and the same object, followed by a numerical reconstruction of the object phase [2,3]. This approach requires several photos being taken from the same sample area and thus increases the possibility of radiation damage. Another approach is the use of energy filtering. By removing the inelastic contributions to the image, a higher contrast and a better signal-to-noise ratio can be reached for the low frequency components [4]. The effect is due to reduction of the background noise. However, a loss of signal still exists as the phase contrast transfer is not affected.

In Fig.3b is shown a picture representing the modulus of the CTF in the two dimensional Fourier space. The modulus of the Fourier transform of a weak phase object image should look in a similar way.

In Fig.4 are shown simulated defocus series of a weak phase object. Simulation conditions: acceleration voltage 300 kV, spherical aberration $C_S = 3$ mm and various defocus. The compromise contrast – resolution is clearly illustrated.

1.1.5. Optimal (Scherzer) defocus.

The so-called optimal (or Scherzer) defocus is defined as the defocus value for which the highest contrast of a point object (atom) is observed [1]. It could be shown that the contrast in the center of an image of a point phase object is proportional to [15 p.219]:

$$I(0) \sim \int_0^{k_A} \sin\left[2\pi\left(-\frac{1}{2}\Delta z \lambda k^2 + \frac{1}{4}C_S \lambda^3 k^4\right)\right] k\, dk, \tag{1.15}$$

where k_A is the aperture cutoff frequency. The above integration can be performed analytically; the result is:

$$I(0) \sim \frac{1}{2}\cos\left(\frac{\pi\,\Delta z^2}{2\lambda C_S}\right)\left[S\left(\frac{\Delta z}{\sqrt{\lambda C_S}}\right) + S\left(-\frac{\Delta z}{\sqrt{\lambda C_S}} + k_A^2\sqrt{\lambda^3 C_S}\right)\right] -$$
$$\frac{1}{2}\sin\left(\frac{\pi\,\Delta z^2}{2\lambda C_S}\right)\left[C\left(\frac{\Delta z}{\sqrt{\lambda C_S}}\right) + C\left(-\frac{\Delta z}{\sqrt{\lambda C_S}} + k_A^2\sqrt{\lambda^3 C_S}\right)\right] \qquad (1.16)$$

where S() and C() are Fresnel integrals.

The definition of optimal defocus requires that the aperture cutoff frequency to coincide with the first intercept of the CTF with the frequency axis. At the position of the latter the CTF phase is equal to 0 (slight underfocus). Solving $\gamma(k) = 0$ (from Eq. 1.4) gives:

$$k_A = \sqrt{2\frac{\Delta z}{C_S\lambda^2}} \ . \qquad (1.17)$$

By substituting Eq. 1.17 in Eq. 1.16 and subsequent numerical optimization of the intensity (for maximum intensity i.e. highest contrast) the value of the optimal defocus is achieved:

$$\Delta z_{CO} = 1.21\sqrt{C_S\lambda} \ . \qquad (1.18)$$

Substitution of Eq. 1.18 into Eq. 1.17 gives the value of the first intercept of the CTF with the frequency axis (cutoff frequency):

$$k_{CO} = \frac{1.56}{(C_S\lambda^3)^{1/4}} \ . \qquad (1.19)$$

In Fig.3a is plotted a curve representing the phase CTF at Scherzer defocus (dashed curve). It can be seen that at this defocus a large portion of the spectrum is transferred with almost no disturbance. However the low frequency components are damped making it inappropriate for biological observations. This is clearly illustrated by the simulated image in Fig.4 ($\Delta z = 93\,\text{nm}$). The Scherzer defocus is of particular importance to material science observations where the object information is below 1 nm spacing thus good transfer of frequencies above 1 nm^{-1} is required.

1.2. Application of Zernike phase plate to TEM (the PTEM) and image formation theory of the PTEM.

1.2.1. The Zernike phase plate.

The phase contrast technique, invented for the light microscopy by Zernike [5], utilizes a phase plate, which shifts the phase of the scattered relative to unscattered waves. The phase plate is positioned at diffraction plane and either advances or retards with π/2 the phase of the zeroth-diffraction beam relative to the scatter.

In electron microscopy phase shifting could be realized by electrostatic or magnetic fields. Such fields however if produced in free space are impossible to restrict to fixed dimension. The inner potential of a material is restricted to the shape of the object and has well defined magnitude. By shaping the material in a proper form it is possible to design the phase shift distribution which will be exerted on the electron waves traversing it. The relation between the phase shift and the material thickness is given by the relativistic formula [12]:

$$\varphi = -\pi \frac{h}{\lambda} \frac{V}{U_0} \frac{1 + 2\alpha U_0}{1 + \alpha U_0} \ , \tag{1.20}$$

where λ is the electron wavelength, h is the thickness, V is the inner potential of the material, U_0 is the acceleration voltage, $\alpha = 0.9785.10^{-6} \ V^{-1}$ is a constant.

In order to realize a Zernike type of phase plate for TEM it is enough to place a thin film at the back-focal plane of the objective lens. The thickness difference between the place where the zeroth-diffraction beam passes and the rest of the film should be ±π/2. The simplest such configuration is shown in Fig.5. The film is with thickness for -π/2 phase shift and in the center there is a small hole. The phase plate is positioned in a way that the zeroth-diffraction beam to pass through the hole. Thus the phase difference between the zeroth-diffraction beam and the scattered waves will be π/2.

Another possibility is to use a phase plate in the form of film of arbitrary thickness with a small circular knob in the center. The knob height above the film surface is calculated for $-\pi/2$ phase shift. The zeroth-diffraction beam passes through the knob and is thus retarded in phase with $\pi/2$ relative to the scattered waves. This configuration however has some major disadvantages compared to the pinhole phase plate. The central thicker part will be exposed to strong electron bombardment by the zeroth-diffraction beam. This will rise such problems as radiation induced contamination and radiation induced electrostatic charging. Another aspect is the production of such phase plate – it is much more difficult to fabricate a knob with precisely defined thickness than to make a hole.

1.2.2. Material for phase plate preparation.

There are two major properties guiding the choice of materials for phase plate preparation – electrical conductivity and electron transparency at thickness for $-\pi/2$ phase shift. Additionally such factors as resistivity to oxidation, ease of preparation and handling, toughness in thin film form and environment friendliness should be considered.

Electrical conductivity of the film is important because high-energy electron bombardment induces much stronger charging in non-conductive materials (there is no electrical path to ground for the charge to escape). If the film is charged a 3-dimensional electrostatic field is formed in the surrounding space, which in turn disturbs the electron wave.

Some of the electrons passing through the film of the phase plate interact with the atoms of the material and are scattered. Such electrons are prevented from contributing to the phase image thus high electron transparency of the film is desirable.

In Table 1 are shown the thicknesses corresponding to $-\pi/2$ phase shift calculated through Eq. 1.20 for different elements at 100 kV and 300 kV acceleration voltages. The inner potential values were taken from the literature

10

[15 p.51]. The heavier elements have higher inner potential so the $-\pi/2$ phase shift thickness is smaller for them. Such elements however are expected to scatter more electrons hence more detailed investigation is necessary.

In Fig.6 is shown calculated electron transparency at thickness for $-\pi/2$ phase shift (from Table 1). Electron transparency is defined as the ratio between unscattered/incident number of electrons. The calculation was performed using empirical model [15 p.202]. Values for inelastic, elastic and total transparency are shown at 100 kV and 300 kV acceleration voltages. The general trend observed is decrease of the transparency with the increase of the element number. Higher acceleration voltage improves the transparency without affecting the qualitative behavior ("scales up" the curves).

Beryllium is one of the elements showing high total electron transparency (73% at 100 kV; 80% at 300 kV). It has been previously proposed in the literature for phase plate preparation [8]. Thin films of beryllium are tough enough to be self-supportive even at very low thickness (20 – 25 angstroms) [18]. Beryllium has high electrical conductivity but on contact with air the surface of the metal oxidizes. The oxide is electrical insulator, which can pose a problem with electrostatic charging of the phase plate. Another restricting factor for the use of beryllium is its high toxicity requiring special precautions during preparation and handling.

Aluminum is also showing high total electron transparency (75% at 100 kV; 82% at 300 kV) regardless of the fact that it is heavier than beryllium. This is due to the high inner potential of aluminum (12.1 V) compared to that of beryllium (7.8 V). The higher inner potential leads to lower $-\pi/2$ phase shift thickness thus improves the electron transparency. Aluminum is non-toxic and is easy to prepare but it shares with beryllium the problem of surface oxidation in air. The preparation of phase plates is yet done manually so avoiding air exposure is very difficult.

Silicon has similar to aluminum total electron transparency (76.5% at 100 kV; 82.9% at 300 kV). The effect of it's higher atomic number and slightly

lower inner potential is compensated by it's lower density (2.33 g/cm^3) compared to aluminum (2.7 g/cm^3). At similar -π/2 phase shift thickness there will be less scattering centers (atoms). Being a semiconductor, in pure form silicon behaves like insulator. In order to become conductive it has to be doped with small amounts of other elements. This together with the possibility of oxidation will complicate the preparation procedure.

Carbon is showing about 10% less electron transparency compared to the previously discussed elements (62.8% at 100 kV; 72.1% at 300 kV). The reason is it's low inner potential and moderate atomic number. Carbon is widely used as specimen support for TEM specimens. It is chemically inert, easy to prepare and forms tough amorphous films even at very low thicknesses (20A). These practical advantages make it more attractive as the material of choice in trial experiments. In our trial the phase plates were prepared using carbon films.

The higher atomic number elements show deteriorating electron transparency so they are not appropriate for phase plate preparation.

There are many other possibilities for phase plate material. Composite materials (alloys) have to be considered. Sandwich type configurations (Carbon – Beryllium – Carbon) could be used for preventing the formation of oxide layers. This is yet an open field, which needs thorough exploration.

1.2.3. Contrast transfer properties of TEM with Zernike phase plate.

At the back-focal plane of the objective lens the real space distance r is related to the spatial frequency k through the following formula:

$$k = \frac{r}{f\lambda} \, , \tag{1.21}$$

where f is the focal length of the objective. The presence of a Zernike phase plate at the back-focal plane with the hole centered on the optical axis could be described through the following phase plate function:

$$\varphi(\vec{k}) = \begin{cases} 0 & ,|\vec{k}| < k_h \\ \varphi_0 & ,|\vec{k}| \geq k_h \end{cases} , \tag{1.22}$$

where φ_0 is the phase shift due to the material film, k_h is the spatial frequency corresponding to the edge of the phase plate hole. The hole cutoff frequency k_h is related to the radius of the hole r_h through (from Eq. 1.21):

$$k_h = \frac{r_h}{f\lambda} . \tag{1.23}$$

The phase shift due to phase plate will be added to that of the CTF so the modulated diffraction wave will become (from Eq. 1.9):

$$\Psi'_p(\vec{k}) = \delta(0) + [\tilde{a}(\vec{k}) + i\tilde{\Phi}(\vec{k})]e^{i\gamma(\vec{k})} e^{i\varphi(\vec{k})} . \tag{1.24}$$

The disturbance to the image wave η will be given by (from Eq. 1.11):

$$\eta_p(\vec{r}) = FT\{[\tilde{a}(\vec{k}) + i\tilde{\Phi}(\vec{k})]e^{i\gamma(\vec{k})} e^{i\varphi(\vec{k})}\} . \tag{1.25}$$

Substitution of Eq. 1.25 in Eq. 1.12 and usage of Fourier transform properties leads to the following equation for the image intensity:

$$\begin{aligned} I_p(\vec{r}) &\approx 1 + 2\operatorname{Re}\left[FT\{[\tilde{a}(\vec{k}) + i\tilde{\Phi}(\vec{k})] e^{i\gamma(\vec{k})} e^{i\varphi(\vec{k})}\}\right] = \\ &= 1 + 2FT\{\tilde{a}(\vec{k})\cos[\gamma(\vec{k}) + \varphi(\vec{k})] - \tilde{\Phi}(\vec{k})\sin[\gamma(\vec{k}) + \varphi(\vec{k})]\} \end{aligned} \tag{1.26}$$

If the phase shift φ_0 (see Eq. 1.22) is equal to 0 (no phase plate) then the above equation matches the one for conventional TEM (Eq. 1.14). In the case of phase shift φ_0 equal to $-\pi/2$ (Zernike phase plate) Eq. 1.26 becomes:

$$I_p(\vec{r}) = \begin{cases} 1 + 2FT\{\tilde{a}(\vec{k})\cos(\gamma(\vec{k})) - \tilde{\Phi}(\vec{k})\sin(\gamma(\vec{k}))\}, & |\vec{k}| < k_h \\ 1 + 2FT\{\tilde{a}(\vec{k})\sin(\gamma(\vec{k})) + \tilde{\Phi}(\vec{k})\cos(\gamma(\vec{k}))\}, & |\vec{k}| \geq k_h \end{cases} . \tag{1.27}$$

For spatial frequencies passing inside the hole there is no change of the contrast transfer. Frequencies passing outside the hole through the film of the phase plate however are transferred through a modified CTF. This new CTF modulates the object wave amplitude with sine function and the object wave phase with cosine function.

In Fig.7 are shown plots of calculated phase CTFs for TEM utilizing Zernike phase plate (PTEM) with infinitely small hole ($k_h \to 0$). The curves

were calculated for acceleration voltage of 300 kV, spherical aberration coefficient $C_S = 3$ mm and different defocus values. Compared to the phase CTFs of the conventional TEM (CTEM) (Fig.3a) the character of the phase contrast transfer is radically changed. Curves at the same defocus for CTEM and PTEM are conjugate in a sense that the zero crossings of the CTEM CTF correspond to unity of the PTEM CTF and vice versa. The PTEM presents very good transfer of the low spatial frequencies without compromising the direct resolution (cutoff frequency). These characteristics of the PTEM make it very attractive for biological observations. In most of such applications it can cover with one photo the whole spectral range of interest. The information transfer characteristics are best at defocus values close to focus but the exact value of the optimal defocus has to be calculated.

1.2.4. Optimal defocus for PTEM.

We will use the same definition as for CTEM for the calculation of the optimal defocus for PTEM (see sect. 1.1.5.). It is easy to show that in the case of PTEM the contrast in the center of an image of a point phase object is proportional to:

$$I_p(0) \sim \int_0^{k_{ap}} \cos\left[2\pi \left(-\frac{1}{2} \Delta z \lambda k^2 + \frac{1}{4} C_S \lambda^3 k^4 \right) \right] k \, dk \ .$$ (1.28)

The integration could be performed analytically, the result being:

$$I_p(0) \sim \frac{1}{2}\cos\left(\frac{\pi \Delta z^2}{2\lambda C_S}\right) \left[C\left(\frac{\Delta z}{\sqrt{\lambda C_S}}\right) + C\left(-\frac{\Delta z}{\sqrt{\lambda C_S}} + k_{ap}^2\sqrt{\lambda^3 C_S}\right) \right]$$
$$ - \frac{1}{2}\sin\left(\frac{\pi \Delta z^2}{2\lambda C_S}\right) \left[S\left(\frac{\Delta z}{\sqrt{\lambda C_S}}\right) + S\left(-\frac{\Delta z}{\sqrt{\lambda C_S}} + k_{ap}^2\sqrt{\lambda^3 C_S}\right) \right]$$ (1.29)

where C() and S() are Fresnel integrals.

The definition of optimal defocus requires that the aperture cutoff frequency coincides with the first intercept of the CTF with the frequency axis.

At the position of the latter the PTEM CTF phase will be equal to $\pi/2$ ($\gamma(k) - \pi/2 = 0$). Solving $\gamma(k) = \pi/2$ (from Eq. 1.4) gives:

$$k_{AP} = \sqrt{\frac{\Delta z + \sqrt{\Delta z^2 + \lambda C_S}}{C_S \lambda^2}} .$$ (1.30)

Substitution of Eq. 1.30 in Eq. 1.29 and subsequent numerical optimization of the defocus Δz for maximum intensity $I_p(0)$ gives:

$$\Delta z_{PO} = 0.73\sqrt{C_S \lambda}$$ (1.31)

for the optimal defocus in the case of PTEM. The first intercept of the PTEM phase CTF with the frequency axis is calculated by substitution of Eq. 1.31 in Eq. 1.30 giving:

$$k_{PO} = \frac{1.40}{(C_S \lambda^3)^{1/4}}$$ (1.32)

for the cutoff frequency at optimal defocus.

Compared to the CTEM the PTEM shows slightly lower values for the optimal defocus and the cutoff frequency. However at optimal defocus it preserves much better the lower part of the frequency spectrum (compare Fig.3a and Fig.7 dashed curves). This presents a big advantage because biological observations could be performed at optimal defocus with the PTEM with much better direct resolution and information transfer efficiency than deeply defocused CTEM.

In practice the hole in the phase plate has finite size which results in a hole-cutoff frequency at the low part of the spectrum. This frequency however is low enough not to impair biological observations of macromolecules as will be shown in the experimental part.

In Fig.8 are shown simulated PTEM images of a weak phase object. Simulation conditions: acceleration voltage 300 kV, objective focal length $f = 3.5$ mm spherical aberration $C_S = 3$ mm, phase plate hole diameter 1μm and various defocus. The images are showing remarkably high contrast compared to CTEM (Fig.4). The overall contrast is not significantly influenced by the defocus

value. Very low frequency modulation is present corresponding to the cutoff frequency of the phase plate hole. The appearance of the images taken at just focus ($\Delta z = 0\,\mathrm{nm}$) and optimal defocus ($\Delta z = 56\,\mathrm{nm}$) is very similar due to the absence of high frequency details in the original object.

1.3. Experimental results of the application of Zernike phase plate to TEM.

1.3.1. Experimental setup.

The experiments were performed on a JEOL JEM-4010N transmission electron microscope operated at 300 kV. This microscope is equipped with LaB_6 electron gun and large gap objective lens polepiece with spherical aberration coefficient of C_S = 3 mm and focal length of f = 3.5 mm. Room temperature side-entry holder was used. The images were captured with GATAN MegaScan 795 2Kx2K CCD camera.

1.3.2. Phase plate preparation.

Because of its practical advantages carbon was chosen as material for phase plate preparation. The films were prepared by evaporation in vacuum (JEOL JEE-400) on a freshly cleaved mica surface. Film thickness was chosen for $-\pi/2$ phase shift at 300 kV (~ 31 nm from Table 1). The films were floated on water surface and picked on standard 50 μm in diameter molybdenum objective lens apertures (3.63 nm^{-1} aperture cutoff frequency; 0.28 nm periodicity). The hole in the center of each phase plate was produced by JEOL JFIB-2300 focused ion-beam machine. The hole diameter was 1 μm corresponding to k-space hole-cutoff frequency of k_h = 0.073 nm^{-1} (13.7 nm periodicity). Our experience from the initial experiments showed that the surface of the carbon film is covered with adsorbed organic molecules which leads to high irradiation induced

16

contamination rates in the microscope. We were not able to surely identify the source of these hydrocarbons. Possible sources are the diffusion pump of the vacuum evaporator or the prolonged exposure to room air. Cleaning procedure with organic solvents was adopted which greatly reduced the contamination. The procedure was: 15 min in xylene; 15 min in dichlorethane; 15 min in methanol. Analytical grade solvents were used. The phase plates were transferred fast from one solvent bath to the next in order to prevent them from drying. After the cleaning and drying the ready phase plates were immediately secured into the objective lens aperture holder and inserted into the microscope.

In Fig.9a is shown an image of the phase plate acquired by the ion beam machine after the hole was produced. In Fig.9b is shown an image of a contaminated phase plate after it has been used in several experiments. Many point-like contamination spots can be seen around the hole, caused by the focused electron beam irradiation. The wide uniformly contaminated area was formed by the illumination with a spread beam. The life-span of a phase plate strongly depends on the apparatus, the preparation procedure and the experimental conditions.

1.3.3. Phase plate application procedures.

After numerous initial experiments in which electrostatic charging and beam induced contamination proved to be basic problems a thorough investigation of the charging phenomenon was performed (see Chapter 2). The results showed that pre-irradiation of the whole area of the phase plate with spread electron beam reduces significantly the magnitude of the charging. The pre-irradiation procedure was adopted as standard step before each experimental session. The microscope was switched to LOW MAG mode (low magnification) and the conditions optimized for highest beam intensity (largest condenser aperture selected, largest spot size, specimen holder out). In LOW MAG mode the objective lens current is switched off and this makes possible the observation

of the whole area of the phase plate. The beam was expanded and the phase plate inserted into the optical path. Beam size was adjusted to cover area slightly larger than the visible aperture opening. This condition was kept for about 30 min during which time the phase plate film receives a dose of approximately $2000 \ e^-/nm^2$. For reduction of the adsorption rate of new contamination-forming molecules, the built-in anticontamination device of the microscope was used during the experiments. In these conditions, the effect of pre-irradiation lasted for several hours. After the pre-irradiation the phase plate was retracted, the specimen holder inserted and the observation session begun.

At the beginning of the observation session a standard microscope alignment procedure was carried out. The microscope used is not equipped with probe-forming lens (mini-condenser lens) so the illumination angle cannot be controlled independently of the beam size. Changing the size of the beam (Brightness, second condenser lens) also changes the illumination angle. This moves the position of the diffraction plane along the z-axis. For each z-axis position of the phase plate and objective lens current there is only one beam size for which the diffraction plane is at the phase plate. Because of this restriction the phase plate z-axis position was adjusted mechanically to match the diffraction plane at the photo-taking conditions (magnification, current density). If for example the beam was then expanded the diffraction plane moves and this results in a visible projection of the phase plate hole on the screen. Phase plate z-axis adjustment was performed if necessary in the beginning of each observation session.

Since the aperture holder drive mechanism is not designed for fine positioning, the XY-centering of the phase plate on the optical axis was carried out in two steps. The microscope was switched to diffraction mode and the phase plate was placed as centered as possible, with the aperture drives. The mechanical centering precision was about 0.3 µm. Then, the microscope was switched back to brightfield imaging mode and fine centering was this time carried out with the beam tilt controls. The maximum tilt correction needed for

18

fine centering was about 0.1 mrad. The observation of a circular edge in the image (hole in the support film or circular particle) helped in the alignment procedure. When the beam is centered in the phase plate hole the wide Fresnel ring corresponding to the hole edge cut-off frequency appears symmetrically around the edge of the object.

Although the main part of the electron beam passes through the hole, the surrounding film is still subjected to strong electron bombardment. The size of the zeroth-diffraction spot depends on the illumination conditions in the microscope and is larger for the LaB_6 electron guns (used in JEM-4010N) compared to the high brightness field emission guns. Inelastic scattering in the specimen can also increase the electron intensity around the central beam. Bombardment of the phase plate results in electrostatic charging of the central area, which in turn distorts the CTF. The charging observed was positive and effectively modified the CTF in a way similar to overfocusing with the objective lens. Thus the deformation due to charging could be partially compensated by the application of slight underfocus. The optimum defocus with the highest cutoff frequency was determined for each experiment by observing the pseudo real-time diffraction image produced by the CCD camera control software (Digital Micrograph). The behavior of the image contrast when changing the defocus seemed very unusual at first. It was opposite to what we are used to observe in conventional TEM. In order to increase the contrast, electron microscopists usually increase the defocus. When the phase plate was used, there was one point where the image was most clear with the highest contrast i.e., the optimal defocus. Changing the defocus resulted in a deterioration of both the resolution and the contrast, similarly to optical microscopy.

1.3.4. Experimental results.

Figs. 10a and b show the moduli of the Fourier transforms of images taken at same defocus (-830nm, overfocus) without and with the phase plate. For

specimen thin amorphous carbon film was used as a weak phase object. Fig.10c shows the rotationally averaged and background subtracted profiles of the diffraction patterns from Figs. 10a and b. A rough comparison of the CTF amplitudes shows about 20% signal reduction in the PTEM image. The phase plate produces cosine-type CTF. Theoretically, the CTEM and the PTEM CTFs should be complementary i.e. the intercept of the conventional sine-type CTF with the frequency axis should coincide with the maxima of the cosine-type PTEM CTF, and vice versa. Due to electrostatic charging however the PTEM CTF is distorted. The distortion is similar in character to overfocusing. This leads to the conclusion that the central part of the phase plate is positively charged.

In Fig.11 are shown images taken from negatively stained horse spleen ferritin molecules, supported by an amorphous carbon film. The phase TEM image (Fig.11a) demonstrates that a very high contrast can be obtained with a resolution cutoff of above the CCD Niquist frequency i.e. 0.41 nm. The compromise between contrast and direct resolution is clearly illustrated by the conventional images. The image with the deepest underfocus (Fig.11b) shows contrast comparable to that of the PTEM image, however, the direct resolution is limited to 2.2 nm. On the other hand, the image closest to the Scherzer defocus (Fig.11d) shows a very low contrast, although the high frequency components are well preserved up to 0.45 nm.

1.4. Discussion.

The improvements in the direct imaging illustrated above, shows that the Zernike phase plate can be successfully applied in TEM. For biological samples, the resolution is limited by the low contrast and the damage caused by the electron bombardment. Avoiding the need for defocus series and post-experimental image processing, will greatly increase the observation efficiency. These benefits, however, are still defeated by the practical difficulties in applying

the technique. Listed below are the main problems associated with the application of the Zernike phase plate in TEM together with possible solutions:

1. The charging of the phase plate, which is considered to be mainly due to contaminants (see Chapter 2) [19] is the major problem encountered in this investigation. Improvement of the vacuum with means of an oil-free vacuum system should greatly reduce the adsorption of organic molecules onto the phase plate. However, this alone will not prevent formation of the contamination layer; it will only extend the time needed for covering the surface with adsorbed molecules [20]. As the phase plate resides inside the microscope for a long period of time, a better solution would be to keep it warm, while not in use. This will prevent adsorption and will reduce contamination drastically. The use of a different material with a higher electrical conductivity (Al, doped Si, composite materials) should reduce the charging of the film itself.

2. The reduction of the signal-to-noise ratio of the image due to scattering from the phase plate may be lessened by using a different material for preparing the phase plate (Al, Si). In the worst case, every information-carrying electron which has been scattered from the plate (elastically or inelastically), is prevented from contributing to the phase image. Such electrons are added to the background of the image. As a result of double scattering (first occurring in the object, then in the phase plate), this contribution to the background is very small. This leads to the conclusion that scattering from the phase plate will deteriorate the image, mainly through a reduction of the number of information-carrying electrons. Implementation of energy filtering aside from removing inelastic scatter from the object will not improve the performance of PTEM. A Boersch's electrostatic phase plate, if successfully realized, should solve the scattering problem [13].

3. The complicated experimental procedures associated with the application of the phase plate could be greatly simplified by the use of computer

control. A piezo-electric or high-precision mechanical aperture drive controlled by a computer should allow for an automatic and precise insertion and retraction of the phase plates. The goal is to simplify the procedure of taking a phase TEM photo to a "press-one-button" operation.

4. The fabrication of phase plates is currently done manually, and involves numerous operations which lowers the success rate. In this respect, the semiconductor industry has a great experience and technology to offer in microfabrication [21].

5. The resolution of the phase TEM images is limited by the cutoff frequency. Higher resolution may be reached combining conventional and phase TEM images. The complex reconstruction process described in Chapter 3 [22, 23] results in an aberration-corrected complex form of the object wave, i.e., the phase and the amplitude parts of the image, and extends the resolution to the information limit of the microscope.

The results presented in this chapter show that a successful application of the Zernike-type phase plate to TEM is possible. Several factors, mainly related to the evolution of the technology, set this work apart from previous phase plate application attempts [6-12]:

1. Focused ion beam (FIB) technique was used for production of the hole in the phase plate. This gives high level of control over the hole shape and allows for preparation of much smaller holes (1 μm diameter) compared to previous attempts (5 μm or larger [6-12]). The smaller diameter of the hole reduces the hole cutoff frequency thus extending the PTEM phase contrast transfer to lower spatial frequencies. This is an important improvement as the main advantage of using a phase plate is the good phase contrast transfer for the low part of the spectrum.

2. The transmission electron microscope used in this investigation is of a much newer generation compared to the machines used is previous trials, done about 30 years ago [6-12]. It employs a turbomolecular vacuum pump

for the specimen area producing much cleaner vacuum compared to diffusion pumps. This reduces the contamination and consequently the electrostatic charging of the phase plate. The LaB_6 electron gun has higher brightness than tungsten filaments producing smaller central diffraction spot. This makes possible the use of a phase plate with smaller hole.

3. For the first time phase plate application experiments are performed using 300 kV electrons. All previous attempts were done at 100 kV or lower acceleration voltages [6-12]. The higher acceleration voltage is advantageous in several ways. The phase plate film thickness for $-\pi/2$ phase shift at 300 kV is about 1.5 times that at 100 kV (see Table 1). Thicker film will have better electrical conductivity, which can reduce electrostatic charging. The scattering cross sections are smaller for higher energy electrons. This reduces the total scattering from the phase plate (see Fig.6). The amount of electrons scattered from the sample will also be reduced. The phase plate will be subjected to less electron bombardment thus the charging and contamination performance will be improved. At higher acceleration voltages the secondary electron yield is less which should also decrease the magnitude of the charging.

4. An in-line CCD camera was used producing pseudo real-time diffractogram of the image (1 frame per second). This helps for finding of optimal defocus condition in the presence of electrostatic charging.

We conclude that most of the practical problems limiting the applicability of the technique that were encountered in this trial, may be solved. Biological electron microscopy will benefit greatly of the phase TEM, if realized. Observation techniques such as ice-embedding and high pressure freezing, where the contrast is a basic problem, are the main candidates subject to possible improvements. If the technique is brought to the level of the current user-friendly and high efficiency instruments, it has a chance to become a standard in the field of biological observations.

2. DIFFERENTIAL ELECTRON INTERFEROMETRY – CHARGE DISTRIBUTION MEASUREMENTS OF THIN FILMS IN TEM

In Chapter 1 was described the application of a Zernike-type phase plate to TEM. The experiments showed that the phase plate is electrostatically charged due to the bombardment of the film by high-energy electrons. As the charging appeared to be a major practical problem in the application of thin film phase plates detailed investigation on the phenomenon was performed.

The charging effect due to electron beam irradiation is a well known and, in most cases, an undesirable effect [24]. The phenomenon was once intensively studied but mainly in relation to scanning electron microscopy (SEM) (see the references in Ref. 25). The conditions in transmission electron microscopy (TEM) are somewhat different in that the specimens are very thin films and the electron energies used are much higher. Detailed description of the process and the resulting macroscopic effects in TEM conditions has been given by Cazeaux [26].

There are few experimental works utilizing electron holography in which the charging of dielectric spheres as well as electric potentials and magnetic fields in solids have been investigated [27-30]. Another application, where electron induced charging is employed, is the electrostatic phase plate proposed by Unwin [31] which uses the potential produced in the central portion of a thin thread placed on a microscope aperture.

Theoretical modeling of the phase shift of electron waves is based on the numerical solution of the Laplace equation for the electric potential with different geometries of the conducting walls and different boundary conditions [25,32]. Krakow and Siegel [33] investigated, both analytically and experimentally, the transfer characteristics of an electrostatic phase plate similar to one described by Unwin [31] as functions of the magnitude of charge and defocus. Such a model was used in Ref. 24 to describe the electric field induced in insulators by electron bombardment. From the solution of the Laplace equation, Matsumoto and

Tonomura [13] proved that the phase shift, which is proportional to the potential integrated along the optical axis, is constant inside the ring of a Boersch-type phase plate. The problem of the determination of the electron wave phase shift becomes more important in thin film phase plates and thin foil lens techniques when the charging effect takes place.

We present a new technique of measuring electron wave phase shift similar to the one proposed by Hoppe (see page 612 in Ref. 9). Using the fact that electron waves traveling through an electrostatic field experience a phase shift, our method exploits the influence on the phase contrast transfer properties of the transmission electron microscope. Placing a charged film at the back-focal plane of the objective lens results in a change of the phase contrast transfer function. Taking two photos of an amorphous weak-phase object with and without film at the back-focal plane, the phase shift by charging is extracted. In Ref. [9] page 611 the phase shift measurement in the back-focal plane of the objective lens is called "interferometry with the electron microscope". Because in our case the difference between two measurements (photos) is used we will refer to this technique as Differential Electron Interferometry (DEI) [19].

In the electron holography [27-30] the phase shift of the electron waves and the electrostatic potential are measured inside the field of the main electron beam. The DEI measures the potential not only inside the irradiated by the main beam area but also outside where the low intensity scattered electrons act as a non-influencing probe beam. The sensitivity is very high allowing for measurements of potentials in the order of hundredths of Volt. However some limitations exist: the specimen should be in the form of thin uniform film with constant thickness and isotropic electric properties; the condition investigated is at electrostatic equilibrium and the currents flowing across the film could not be observed.

The theoretical modeling of the phase shift of electron waves is based on the numerical solution of the Laplace equation for the electric potential using a variety of geometry of the conducting walls and boundary conditions for the

electric potential at them [24, 25, 32, 33]. Similar problems appear when a foil lens is applied to the objective lens of a conventional transmission electron microscopy in order to improve the electron probe profile [34, 35]. All these theoretical work have not given idea about the solution of the inverse Laplace problem, which is important for the reconstruction of the physical parameters from experimental data. From mathematical viewpoint the solution of the inverse Laplace problem is much easier if the boundary conditions for the potential at surfaces are postulated. Then for example the surface potential at the irradiated film can be reconstructed. Unfortunately, this solution will not be a great success because in order to find the surface charge the second derivative from the reconstructed data has to be taken. It is well known fact that the error in the second derivative of the experimental type curves is very large and some times it is not possible to extract any information. Therefore, the inverse Laplace problem has to be solved for the direct reconstruction of the surface charge distribution.

This Chapter is outlined as follows. In Sec. 2.1 the experimental results for the phase difference between the contrast transfer functions of two photos taken with and without film at the back-focal plane are described. The measured normalized electron beam intensity gives additional information about the geometry of the charging area. The solution of the inverse Laplace problem for the reconstruction of the electric charge density is developed in Sec. 2.2. The phase shift of electron waves is derived in a weak lens approximation. With this method the radial dependence of the charge density and the magnitude of the electrostatic potential at the thin film is obtained in Sec. 2.3.

2.1. Experimental data.

2.1.1. Differential Electron Interferometry.

The film being investigated experimentally is placed on the standard objective lens aperture (see Fig.12). The aperture is positioned at the back-focal plane of the objective lens and centered so that the strong central beam of unscattered electrons passes through the central portion of the film. Amorphous carbon film is placed at the specimen plane producing a uniform distribution of scattered electrons. The intensity of the central beam is several orders higher, than that of the scattered ones allowing for the assumption that charging takes place mainly in the central area.

In the weak phase object approximation, the phase contrast transfer of the microscope is described by the contrast transfer function $\sin[\gamma(k) + \varphi(k)]$ multiplying the Fourier transform of the object wave. Here $\varphi(k)$ is the phase shift due to charging and $\gamma(k)$ is the one due to defocus and spherical aberration (Eq. 1.4).

From the Fourier transform of an image it is possible to extract the total phase shift as a function of k by fitting the positions of the extrema in the transfer function [19]. Then, if all the parameters in Eq. 1.4 are known, $\varphi(k)$ can be evaluated. Using Eq. 1.21 the real space dependence $\varphi(r)$ is calculated. Important requirement is that the phase shift due to charging or due to some varying properties of the film to have axial symmetry.

The DEI has the advantage that it allows for measurement of the potential not only inside the illuminated area but also in the outside area where scattered electrons pass. It is very sensitive allowing for measurement of low surface potentials. On the other hand this could cause problems with rapidly changing or very high potentials in the case of insulating films. The required density of experimental points for the whole range covering the decay of the contrast

transfer function (CTF) can be met by combining the data from several photos taken at different defocus Δz.

The extraction of the phase shift due to charging is illustrated in Fig.13. The phase shift from each photo is extracted by fitting the positions of the extrema in the rotationally averaged CTF profile. The phase step between two adjacent extrema (minimum and maximum) is $\pi/2$. In our experiments the material film is usually charged positively due to the emission of secondary electrons exceeding the amount of the captured. This gives effect similar to overfocusing because the central portion of the electron wave at the back-focal plane retards relatively to the outer part. Taking the photos at overfocus condition ($\Delta z < 0$) gives the advantage of easier processing of the data. In this case the phase shift in the CTFs is positive and it increases monotonously.

2.1.2. Experimental setup and procedures.

For our experiments we used JEOL JEM-4010N transmission electron microscope with LaB_6 gun operated at 300 kV ($C_S = 3$ mm). Amorphous carbon film with thickness 32 ± 1 nm was prepared by vacuum evaporation on freshly cleaved mica, floated on water and transferred on standard 50 μm molybdenum apertures. The apertures were then placed in the objective lens aperture holder and inserted into the microscope. The aperture holder was positioned slightly below the back-focal plane giving more spread central beam on the film. In order to reduce the effects of contamination we used the microscope's built-in anticontaminator in all experiments.

In our trial experiments we observed a change of the charging properties of the film due to the irradiation of the film by the electron beam. In the literature the characteristic time for the charge to reach equilibrium is given in the order of several seconds [24]. We could not observe this initial charge buildup as it is too fast for our experimental technique. However a decrease in the charge magnitude

was observed after the film was irradiated for minutes. In order to investigate this effect three measurements of the phase shift due to the charging were performed – without pre-irradiation, after 30 minutes pre-irradiation and after 30 more minutes or total of 60 minutes pre-irradiation. In the literature [36] a reduction of the contamination rate after pre-irradiation has been reported, which could be related to the charging behavior.

Each measurement consisted of 4 photos: two defocus values and two photos at each defocus – one with film and one without film at the back-focal plane. Combining the data from several defocuses increases the number of data points thus improving the statistics. The pre-irradiation was performed by spreading of the electron beam so that the whole aperture opening to be covered by the beam. Pre-irradiation of 30 minutes gives a total dose of around 2000 e^-/nm^2 to the film. After each pre-irradiation the aperture is retracted and left for 5 minutes outside the beam. This procedure is used for temperature stabilization and relaxation of short-time processes before the photos are taken. The photographic exposure was 2 seconds with beam current of around 6.10^{-9} A (measured with the microscope's built-in electrometer).

The charge distribution of the measured film is expected to correlate with the radial dependence of the electron beam intensity. Hence, we pay a special attention for the measurement of the beam intensity distribution. The beam profile at the film was measured in diffraction mode by focusing on the aperture and taking a snapshot with an inline 2Kx2K CCD camera. The CCD camera was not used for the phase shift measurement as it offers much lower total pixel number compared to the photographic film (i.e. lower signal-to-noise ratio in the CTF data).

2.1.3. Experimental results.

The results for the phase shifts from the three measurements are given in Fig.14. Each plot also includes the measured beam profile normalized through its

maximum intensity. The illustrated phase shift datasets are combination from measurements at two defocuses – open and filled symbols. The corresponding values of the defocuses are given in the legends of Figs.14a-c. From the plots it is seen that the difference between the experimental points, obtained at the two defocuses, is small. The dashed line in Figs.14a-c represents the best polynomial fit for each dataset. We used only polynomials of even powers of the radial distance. This requirement comes from the symmetry of the Laplace problem in cylindrical coordinates (see Section 2.3 for details about the data processing). The final conclusion from the experimental data is: the first pre-irradiation (30 minutes) reduces the phase shift due to charging about 2 times (compare Fig.14a and Fig.14b); further irradiation has no significant effect on the phase shift (compare Fig.14b and Fig.14c).

The phase shift measurements are giving some quantitative information about the magnitude of the total charge trapped in the specimen. The larger the phase shift due to the charging the larger the total charge in the specimen. Moreover the radial dependence of the measured phase shift contains information about the radial distribution of this charge. To extract this information the inverse Laplace problem has to be solved.

2.2. Theoretical model for the reconstruction of the surface charge density.

2.2.1. Inverse Laplace problem for the surface charge density.

In order to reconstruct the film charge density ρ from the experimental data, presented in Section 2.1, the inverse Laplace problem for the electric potential function is solved. We will consider the case of axial symmetry and thin films when ρ depends only on the radial coordinate r. The electrostatic potential function at the phase-plate U is a solution of the one-dimensional Poisson equation [24]

$$\frac{1}{r}\frac{d}{dr}\left(r\frac{dU}{dr}\right)=-\frac{\rho}{\varepsilon_0\varepsilon_r} \qquad \text{for} \quad 0\le r\le r_c, \tag{2.1}$$

where ε_0 is the dielectric constant, ε_r is the relative dielectric permittivity of the film and r_c is the radius of the boundary between the conductive and charged film parts. Generally, r_c should be equal to the radius of the aperture r_a, but the experimental results reported in Ref. 19 show that in some cases $r_c < r_a$. In such cases the charging occurs mainly at the surface of the film where some contamination could reside. Then the film is assumed to be conducting and the contamination layer acts as an insulating covering.

We will consider the spatial dependence of the electrostatic potential function, $V(r,z)$, in the case of axial symmetry, where the vertical axis Oz of the cylindrical coordinate system coincides with the axis of symmetry and the film coincides with the zero-plane, $z = 0$ (see Fig. 12). The film separates the calculation area in two parts. The semi-infinite region above the aperture, called here "area I", is described by $z \ge 0$. The region below the film is a cylinder with radius r_a and depth d_a, given by $0 \le r \le r_a$ and $-d_a \le z \le 0$, called "area II". The typical apertures used in TEM have depths more than two times larger than their inner diameter. Therefore, the assumption that the phase shift of the electron wave does not depend on the aperture depth can be applied.

In the case of axial symmetry the electrostatic potential function V is a solution of the two-dimensional Laplace equation [25]:

$$\frac{1}{r}\frac{\partial}{\partial r}\left(r\frac{\partial V}{\partial r}\right)+\frac{\partial^2 V}{\partial z^2}=0 \tag{2.2}$$

in the working areas I and II. The partial differential equation (2.2) is solved using Eq. (2.1) and the boundary conditions that at the aperture wall the electrostatic potential function is zero and it vanishes at infinity.

Knowing the electric potential in the whole region the phase shift φ of the electron wave due to the charging of the film can be estimated in a weak lens approximation [13, 19, 37] as:

$$\varphi(r) = -\pi \frac{1+2\alpha U_0}{1+\alpha U_0} \frac{1}{\lambda U_0} \int_{-\infty}^{\infty} V(r,z)dz + \varphi_f(r), \qquad (2.3)$$

where λ is the electron wavelength, U_0 is the accelerating voltage, and $\alpha = 0.9785.10^{-6} \text{ V}^{-1}$. In Eq. (2.3) $\varphi_f(r)$ is the phase shift of the electron wave corresponding to the internal potential V_{in} and the surface potential $U(r)$. $\varphi_f(r)$ is calculated using the simple formula:

$$\varphi_f(r) = -\pi \frac{1+2\alpha U_0}{1+\alpha U_0} \frac{h}{\lambda U_0} [U(r)+V_{in}]. \qquad (2.4)$$

The internal potential V_{in} is an intrinsic property of the specimen material. As it was shown in the literature [19, 37] for thin films the phase shift calculated from the electrostatic potential in the working area is two orders of magnitude larger than the part of φ_f corresponding to surface potential U. (The typical thickness of the film is $h \approx 30$ nm and the radius of the electron beam is from 5 to 10 μm.) Therefore, the integral in Eq. (2.3) should give the radial dependence of φ, shown in Fig. 14.

2.2.2. Step-wise approach.

The problem (2.1)-(2.3) has no analytical solution and the classical numerical methods are also not applicable [38]. For that reason we will use the idea of the boundary integral method [38]. Following this idea the interval $[0, r_c]$ is divided in N subintervals by points $r_0 = 0$, r_1, ..., $r_N = r_c$. The unknown charge density function ρ divided by the relative permittivity ε_r is represented as a sum of unit step-wise model functions (see Fig. 15) with amplitudes $\rho_k \equiv \rho(r_k)/\varepsilon_r(r_k)$, $k = 1, 2, ..., N$. Then the surface potential function U_k

which corresponds to the *k*-step-wise charge function is a solution of the one-dimensional equation (2.1). The final results read: for $U_1(r)$

$$\frac{4\varepsilon_0 U_1}{\rho_1 r_1^2} = 1 + 2\ln(\frac{r_c}{r_1}) - \frac{r^2}{r_1^2} \quad \text{for} \quad 0 \le r \le r_1,$$

$$\frac{2\varepsilon_0 U_1}{\rho_1 r_1^2} = \ln(\frac{r_c}{r}) \quad \text{for} \quad r_1 \le r \le r_c;$$ (2.5)

and for all other surface potential functions $U_k(r)$ ($k = 2, 3, \ldots, N$)

$$\frac{4\varepsilon_0 U_k}{\rho_k(r_k^2 - r_{k-1}^2)} = 1 + \frac{2r_k^2}{r_k^2 - r_{k-1}^2}\ln(\frac{r_c}{r_k}) + \frac{2r_{k-1}^2}{r_k^2 - r_{k-1}^2}\ln(\frac{r_{k-1}}{r_c}) \quad \text{for}$$

$$0 \le r \le r_{k-1},$$

$$\frac{4\varepsilon_0 U_k}{\rho_k(r_k^2 - r_{k-1}^2)} = \frac{r_k^2 - r^2}{r_k^2 - r_{k-1}^2} + \frac{2r_k^2}{r_k^2 - r_{k-1}^2}\ln(\frac{r_c}{r_k}) + \frac{2r_{k-1}^2}{r_k^2 - r_{k-1}^2}\ln(\frac{r}{r_c}) \quad \text{for}$$

$$r_{k-1} \le r \le r_k,$$

$$\frac{2\varepsilon_0 U_k}{\rho_k(r_k^2 - r_{k-1}^2)} = \ln(\frac{r_c}{r}) \quad \text{for} \quad r_k \le r \le r_c.$$ (2.6)

Because of the linearity of the Laplace equation (2.2) the solution of the problem for the electric potential function can be presented as a superposition of the simpler problems, corresponding to each step-wise charge function. This model gives a very high efficiency of the numerical computations only when the simpler problem has an analytical solution [38]. Otherwise the numerical method is equivalent to the classical difference methods. Fortunately, the particular Laplace problems have simple solutions. For the first surface potential function, $U_1(r)$, the corresponding space dependence of the electric potential function $V_1(r,z)$ and the corresponding radial dependence of the phase shift $\varphi_1(r)$ are reported in Ref. 19.

The analytical solutions of the Laplace equation in the areas I and II are different because of the different boundary conditions at the aperture wall. In the

area I the general solution of Eq. (2.2) is presented, applying the Fourier-Bessel integral transformation [25], as:

$$V_k = \frac{\rho_k(r_k^2 - r_{k-1}^2)}{4\varepsilon_0} \int_0^\infty \tilde{U}_k(s)\exp(-s\frac{z}{r_c})J_0(s\frac{r}{r_c})sds, \qquad (2.7)$$

where J_n is the Bessel function of the n-th order, $\tilde{U}_k(s)$ is the Fourier-Bessel transform of the dimensionless electrostatic potential function at the zero-plane, and $V_k(r,z)$ is the electrostatic potential function corresponding to the k-step-wise charge distribution. The negative sign in the exponent of the solution (2.7) is used in order to satisfy the boundary condition at infinity, i.e. the electrostatic potential function is assumed to be zero at $z \to \infty$. If the boundary condition (2.6) is substituted into the general solution (2.7) and the inverse Fourier-Bessel transformation is taken then the analytical result for the image $\tilde{U}_k(s)$ can be calculated. Using the similar mathematical procedure as in Refs. 19 and 37 the final result can be written in the following form:

$$\tilde{U}_k(s) = \frac{2}{s^2}\{\frac{r_k^2}{r_k^2 - r_{k-1}^2}[J_2(s\frac{r_k}{r_c}) + J_0(s\frac{r_k}{r_c})] -$$

$$-\frac{r_{k-1}^2}{r_k^2 - r_{k-1}^2}[J_2(s\frac{r_{k-1}}{r_c}) + J_0(s\frac{r_{k-1}}{r_c})] - J_0(s)\} \qquad (2.8)$$

for $k = 1, 2, ..., N$. For $k = 1$, $r_0 = 0$, and $r_1 = a$, where a is the measure of the electron beam radius used in Ref. 19, the formula (2.8) gives the respective result for the Fourier-Bessel image from Ref. 19.

In the area II the general solution of the Laplace equation (2.2) for the electrostatic potential function $V_k(r,z)$ is presented as a Fourier-Bessel series [25]

$$V_k = \frac{\rho_k(r_k^2 - r_{k-1}^2)}{4\varepsilon_0} \sum_{i=1}^\infty A_{ki} \exp(\alpha_i \frac{z}{r_a})J_0(\alpha_i \frac{r}{r_a}), \qquad (2.9)$$

where α_i is the i-th zero of the Bessel function J_0, i.e. $J_0(\alpha_i) = 0$ and A_{ki} are constants, which are determined from the boundary condition at the film surface.

This form of the solution obeys the boundary conditions at the aperture wall and at infinity (see Ref. 19). For the constants A_{ki} after the substitution of Eq. (2.6) into Eq. (2.9) and taking into account the orthogonality of the Bessel functions with respect to their zeros the following relationship is derived:

$$A_{ki} = \frac{4}{\alpha_i^2 J_1^2(\alpha_i)} \{ \frac{r_k^2}{r_k^2 - r_{k-1}^2}[J_2(\alpha_i \frac{r_k}{r_a}) + J_0(\alpha_i \frac{r_k}{r_a})] -$$

$$- \frac{r_{k-1}^2}{r_k^2 - r_{k-1}^2}[J_2(\alpha_i \frac{r_{k-1}}{r_a}) + J_0(\alpha_i \frac{r_{k-1}}{r_a})] - J_0(\alpha_i \frac{r_c}{r_a}) \}, \tag{2.10}$$

for $k = 1, 2, ..., N$ and $i = 1, 2, ...$ For $k = 1$, $r_0 = 0$, and $r_1 = a$ the formula (2.10) gives the respective result for the coefficients of the Fourier-Bessel series from Ref. 19.

Because of the linearity of the problem the main part of the phase shift of electron waves due to the charging of the film can be presented as a superposition of the phase shifts φ_k corresponding to each k-step-wise charge distribution. Therefore,

$$\varphi = \varphi_1 + ... + \varphi_N, \qquad \varphi_k(r) = -\pi \frac{1 + 2\alpha U_0}{1 + \alpha U_0} \frac{1}{\lambda U_0} \int_{-\infty}^{\infty} V_k(r,z)dz. \tag{2.11}$$

If the general solutions (2.7) and (2.9) are substituted in Eq. (2.11) the phase shift function φ_k can be calculated:

$$\varphi_k(r) = \pi \frac{1 + 2\alpha U_0}{1 + \alpha U_0} \frac{r_a(r_k^2 - r_{k-1}^2)}{2\lambda U_0}(f_{I,k} + f_{II,k})\rho_k. \tag{2.12}$$

where the dimensionless phase shift factors of the areas I and II are $f_{I,k}$ and $f_{II,k}$, respectively. The phase shift factors are calculated from the relationships

$$f_{I,k} = -\frac{r_c}{2r_a} \int_0^{\infty} \tilde{U}_k(s)J_0(s\frac{r}{r_c})sds, \qquad f_{II,k} = -\frac{1}{2}\sum_{i=1}^{\infty} \frac{A_{ki}}{\alpha_i} J_0(\alpha_i \frac{r}{r_a}). \tag{2.13}$$

The integral, appearing in Eq. (2.13) has an analytical form, which is more convenient for the numerical calculations than the integral representation [39].

The function multiplying ρ_k in Eq. (2.12) corresponds to the unit charge step-wise distribution and they are universal for the problem. Therefore, if we know the experimental data for the phase shift (see Fig. 14) the inverse Laplace problem is transformed to a simple linear optimization procedure for the amplitudes ρ_k.

2.3. Results and discussion.

2.3.1. Direct vs. polynomial interpolated experimental data processing.

Our numerical investigation shows that even six intervals of the charge density are enough to achieve good agreement between the experimental points and the theoretical phase shift function. The numerical results for the phase shift function in the case of Fig. 14a and six charge intervals are plotted in Fig. 16a. Therein the best polynomial fit of the experimental data is also drawn. The difference between them is very small and practically both curves coincide. The corresponding charge density step-wise functions are illustrated in Fig. 16b (bar graph). Further increase of the number of intervals N leads only to appearance of false oscillations in the final results because the procedure assumes precise input data.

In order to find a smooth charge density distribution one can interpolate the found six steps (Fig. 16b). This way is not preferable because we do not have any prior knowledge of the behavior of the charge density. Another possibility is to approximate the original experimental data with a smooth curve. Then substituting this curve (shown in Fig. 14a) as input data we recover the charge density distribution represented by large numbers of intervals. The resulting charge density function is plotted in Fig. 16b (solid line). It is well illustrated that the solid line follows the results from the six charge-steps reconstruction. From our viewpoint interpolation of the original data is more physical because the

decision about the quality of the approximation in the experimental data space is easier.

It is important to know that in the case of axial symmetry the solutions depend on r^2 and the interpolation of the experimental data has to be done also as a function of r^2. In all cases calculated below we compared the results from both approaches and found a good agreement between them (similar to that shown in Fig. 16).

2.3.2. Surface potential and charge distributions.

The calculated distributions of the electric potential at the zero-plane are plotted in Fig. 17a. The different style of lines corresponds to the experimental data for different pre-irradiation times (see Figs. 14a-14c). The calculated radius at which the surface potential becomes zero is about 19 μm in all cases. The surface potential is positive which means that the irradiated film is positively charged. The magnitude of the surface potential in the center of the film is very low about 100 mV. It drops down with increasing of the radial distance for all experiments. The surface potential changes significantly after the first 30 min of the pre-irradiation. Its maximum in the center of the electron beam decreases from 176 mV to 101 mV. Pre-irradiating the film for 30 more minutes (or total of 60 min.) results in a much smaller change (it drops to 92.6 mV). This indicates that the system approaches equilibrium and further pre-irradiation will not significantly influence the surface potential. It is important to note that the type of the curves for the surface potential is similar to the one for the phase shift. Therefore, the surface potential distribution is not very informative about the charging effect.

The reconstructed charge density, $\rho_k \equiv \rho(r_k)/\varepsilon_r(r_k)$, distributions from the experimental data are plotted in Fig. 17b. For better illustration of the correlation between the charge density distribution and the electron beam

intensity the measured normalized intensity is also given in Fig. 17b. It should be noted that the material properties of the film and the real charge density are not known. They both can vary as a function of the electron beam intensity and the time of pre-irradiation. Therefore, we can make quantitative conclusions only for the ratio $\rho_k \equiv \rho(r_k)/\varepsilon_r(r_k)$, which we call "charge density".

The radial distributions of the charge density without pre-irradiation and after 30 and/or 60 minutes pre-irradiation are extremely different (Fig. 17b). Without pre-irradiation the charged area is larger than in the other two cases and the charge density distribution is more spread. In this case there is no visible correlation between the charge density and the electron beam radial dependencies. After the pre-irradiation the charge distribution becomes narrower and in the central part of the film correlates very well with the electron beam profile.

For this complex behavior of the charge density a simple physical explanation could be given if the dielectric permittivity is constant $\varepsilon_r(r_k) = \varepsilon_r$ [15 p.490, 40]. We assume that there is a uniform contamination layer residing on the film surface before the first measurement. As a rule the intensity of the electron beam does not change significantly between the different measurements. The following three processes take place: adsorption/desorption of species on/from the film surfaces, induction of surface charge due to the irradiation, and surface charge diffusion. The diffusion of the charge due to the high mobility of the molecules in the contamination layer results in charge redistribution in the first measurement.

The pre-irradiation has the effect of "fixation" of the hydrocarbon molecules adsorbed on the surface. The second measurement shows localization of the charge around the beam with pronounced "bump" close to the beam edge. This bump is a result of newly adsorbed and diffusing molecules on the surface coming into the vicinity of the irradiated area and being fixed. This ring-type contamination in the case of uniform beam intensity is described in Ref. 15.

3. EXPERIMENTAL REALIZATION OF THE COMPLEX OBSERVATION

Recently in the literature [22] a new scheme for reconstruction of the object wave in its complex form has been proposed. The scheme named "complex observation" utilizes two images, one CTEM and one PTEM, to reconstruct the wave.

In Fig.18 is shown a sketch illustrating the reconstruction process. Two images taken of the same sample area, one without and one with Zernike phase plate, form the input pair. The CTEM image is added to the multiplied by the imaginary unit i PTEM image. Then CTF inverse filter is applied. The result is a modulation-free complex representation of the object wave containing both the amplitude and the phase of the object wave.

There are other techniques for reconstruction of the complex object wave. Electron holography [41, 42] is widely used for high resolution observation in material science. However it is not suitable for biological observations because of the high electron doses required [43]. Defocus series [2, 3, 44] are currently used for observation of biological samples. In this approach several (3 or more) photos are taken from the same sample area thus from a radiation damage point of view the complex reconstruction is superior.

In this chapter we present the first practical realization of the complex reconstruction scheme. Section 3.1. presents some improvements to the originally proposed scheme. Section 3.2. contains experimental results and discussions.

3.1. Improvements to the original "Complex Observation" scheme.

3.1.1. Case of phase shift not equal to -π/2.

The observation scheme proposed by Nagayama [22] could be expanded for the more general case when the phase shift of the phase plate is not exactly -π/2.

Let us consider a PTEM utilizing a chargeless phase plate with arbitrary phase shift φ_0. In a weak object approximation the CTF modulated image wave will then be given by:

$$\psi_{MOD}(\vec{r}) = C_{CTEM}\ I_{CTEM}(\vec{r}) + C_{PTEM}\ I_{PTEM}(\vec{r})\ ,\qquad (3.1)$$

where $I_{CTEM}(\vec{r})$ and $I_{PTEM}(\vec{r})$ are the intensities of the CTEM and PTEM images respectively, both taken at the same defocus. The coefficients C_{CTEM} and C_{PTEM} will depend on the phase shift φ_0 and should satisfy the condition of correct reconstruction of the object wave. It could be easily shown that the appropriate functions are:

$$C_{CTEM} = 1 + i\,\frac{\cos\varphi_0}{\sin\varphi_0}\ ,\qquad (3.2)$$

$$C_{PTEM} = -\frac{i}{\sin\varphi_0}\ .\qquad (3.3)$$

Substitution of $I_{CTEM}(\vec{r})$ from Eq. 1.14, $I_{PTEM}(\vec{r})$ from Eq. 1.26, C_{CTEM} and C_{PTEM} in Eq. 3.1 and subsequent simplification gives:

$$\psi_{MOD}(\vec{r}) = 1 + i\,\frac{\cos\varphi_0 - 1}{\sin\varphi_0} + 2\,FT\{[\tilde{a}(\vec{k}) + i\tilde{\Phi}(\vec{k})]e^{i\gamma(\vec{k})}\}\ .\qquad (3.4)$$

This is the complex form of the CTF modulated image wave. Fourier transform, multiplication with the inverse CTF $e^{-i\gamma(\vec{k})}$ and inverse Fourier transform will result in demodulated complex form of the object wave:

$$\psi_{CR}(\vec{r}) = \left(1 + i\,\frac{\cos\varphi_0 - 1}{\sin\varphi_0}\right) + 2a(\vec{r}) + i2\,\Phi(\vec{r})\ .\qquad (3.5)$$

Simple mathematical manipulations (addition of constant, division by 2) of Eq. 3.5 give the complex object wave:

$$\psi(\vec{r}) = 1 + a(\vec{r}) + i\Phi(\vec{r})\qquad (3.6)$$

(compare with Eq. 1.8).

If the phase shift φ_0 is equal to $-\pi/2$ the coefficients C_{CTEM} and C_{PTEM} become 1 and i respectively, which coincides with the originally proposed reconstruction scheme [22].

3.1.2. Off-plane scheme – a new application scheme for the Zernike phase plate.

The electrostatic charging was recognized in Chapter 1 as the major prectical problem in the application of the Zernike phase plate. The charging deforms the CTF by introducing additional frequency-dependant phase shift investigated in Chapter 2. This makes impossible the application of the complex reconstruction, which requires two images with matched CTFs differing only by a constant phase shift.

In order to satisfy this requirement a new application scheme for the phase plate was developed [23]. The original complex reconstruction scheme will be referred to as on-plane scheme (Fig.19a,b phase plate at the back-focal plane). In the newly developed scheme the phase plate is positioned off the diffraction plane hence the name off-plane scheme (Fig.19c,d). With the off-plane scheme both images for the complex reconstruction are taken with the phase plate in the beam path The first image, resembling CTEM, is taken with the phase plate shifted slightly off-center (Fig.19c). . The second image, resembling PTEM, is taken with the phase plate hole centered on the optical axis (Fig.19d).

In Fig.20 is shown a geometrical optics illustration of on-plane and off-plane schemes. The phase plate in the on-plane scheme (Fig.20a) is positioned at the diffraction plane so the phase shift introduced, between the zeroth-diffraction beam and the scattered electrons, is equal for the whole image. When the phase plate is shifted from the back-focal plane (Fig.20b) the phase shift difference between the zeroth-diffraction beam and the scattered waves will depend on the position in the image. For the central part of the image the zeroth-diffraction passes through the phase plate hole whereas the scattered waves pass through the film. There, a vignette projection of the hole is observed. Inside this projection the image will show a PTEM-like CTF. For a point outside the hole projection the zeroth-diffraction beam together with the majority of the scattered waves pass through the film of the phase plate. This gives no phase shift difference so in this

area the image will show a CTEM-like CTF. There will be a small disturbance in the spectrum corresponding to the projection of the hole on the diffraction plane, but it is not expected to influence the image significantly.

The absolute CTF charging deformation will be stronger with the off-plane scheme, due to zeroth-diffraction beam hitting the phase plate. However, both images are taken with the phase plate in the beam path so this deformation will be identical. The small displacement of the phase plate introduced between the two photos will not influence the charge configuration. This will allow for the application of the complex reconstruction scheme, because the CTFs of the images will be complementary.

3.1.3. Phase shift measurement.

The off-plane scheme allows for phase plate phase shift measurements with precision around 0.05π. Because the charge-induced phase shift is identical in both CTFs the only difference between the CTF phases will be the phase shift due to the phase plate film.

In Fig.21 is shown an example of phase plate phase shift measurement. The upper plot (Fig.21a) shows the rotationally averaged and background subtracted CTF profiles. The positions of the extrema in the profiles are fitted and appropriate phases are assigned to them (for several extrema illustrated by dotted lines). In this way the CTF phase shift data is achieved (Fig.21b). The CTEM CTF phase shift (solid rectangles) is then fitted with polynomial with zero for the free term (from the requirement to be zero at $k = 0\ \text{nm}^{-1}$). The PTEM data (hollow rectangles) is consequently fitted by vertically shifting the so determined polynomial curve (fitting only the free term, the rest of the coefficients are fixed). The amount of shift needed for the best fit is the phase plate phase shift.

3.1.4. CTF demodulation.

For the inverse CTF filtering the CTF has to be determined. Because of the charge-induced deformation the conventional CTF formula (Eq. 1.4) cannot be used for the purpose. One possibility is to use polynomial fitting of the CTF phase as described above. The CTF profiles are usually not very smooth curves. This introduces errors in the extrema positions determination and subsequently in the polynomial approximation.

Another possible approach is based on the so-called approximate phase object (APO) assumption. In the literature reconstruction scheme based on APO has been applied to electron holograms [45]. The object is assumed to show pure phase contrast i.e. no disturbance in the amplitude part of the wave. Numerical optimization procedure is used which minimizes the standard deviation of the amplitude in the reconstructed wave by varying the parameters of the reconstruction.

We developed reconstruction procedure based on APO for the inverse CTF filtering in the complex reconstruction. The extrema positions in the CTF profile are used as initial approximation in the APO optimization procedure. Between these points the phase is interpolated by cubic spline interpolation. The numerical procedure performs multiple Monte Carlo optimization steps and by varying the extrema position parameters minimizes the standard deviation of the reconstructed amplitude image. After sufficient number of iterations the amplitude standard deviation stabilizes showing that the best fit has been reached.

3.2. Results and discussion.

3.2.1. Experimental setup and procedures.

The experimental setup used is the same as for the experiments in Chapter 1. The microscope was operated at 100 kV (complex reconstruction of tobacco mosaic virus) and 400 kV (complex reconstruction of horse spleen ferritin). Carbon film phase plates with appropriate thicknesses (from Eq. 1.20) for 100 kV and 400 kV were prepared (22 nm for 100 kV, 34 nm for 400 kV). The phase plate position inside the microscope was shifted slightly downwards on the z-axis to allow for the application of the off-plane scheme. Insertion and centering of the plate in this case was much easier, because a projection of the hole is seen on the microscope screen.

The off-plane pairs were taken as follows. For the first photo the phase plate was positioned so that the hole projection to be in the center of the screen. After the first photo is taken the phase plate was shifted so that the hole projection to be just outside the area covered by the photographic film. Then the second photo was taken. After the second photo the phase plate was retracted from the beam path.

The image processing and complex reconstruction was performed by homebrew scripts executed on the Digital Micrograph (Gatan Inc.) software platform.

3.2.2. Experimental results.

Fig.22 shows the results from the complex reconstruction of negatively stained horse spleen ferritin and a schematic of the reconstruction process. The complex pair images were taken at 400 kV acceleration voltage at -765 nm overfocus and showed phase shift of $(-0.38\pm0.03)\pi$ (Fig.22a,b). Fourier transformation yields the two CTF-modulated Fourier images (Fig.22c,d), which

are complex-combined and subsequently demodulated (corrected) by means of an inverse filter (Fig.22e). After a second Fourier transform, the CTF-corrected complex image is obtained and the phase and amplitude components are separated (Figs.22f,g). The phase image exhibits high contrast and carries most of the information, while the amplitude image consists mainly of noise. Due to the elimination of CTF-modulation, fine structures of iron oxide cores are clarified in the reconstructed phase image (Fig.22f) as compared with the PTEM image (Fig.22a). A projection of the phase plate hole is seen close to the center in the Fourier transform of the CTEM image (Fig.22d). It is mirrored on both sides because only the wave intensity is registered in the image. This disturbance is close to the center of the diffraction so it is transferred to the amplitude part of the reconstructed wave. There it could be seen as very low frequency modulation in the picture (Fig.22g).

Negatively stained tobacco mosaic virus (TMV), which possesses a periodic structure, was studied by complex EM at 100kV (Fig.23). The complex pair images were taken at -2200 nm overfocus and showed phase shift of $(0.48 \pm 0.05)\pi$. In Fig.23b (PTEM image) is seen the projection of the phase plate hole. The squares in Fig.23a,b indicate the area subjected to complex reconstruction.

In Fig.24a,b are shown the reconstructed amplitude and phase components. Below each picture a diffractogram is shown of selected area and scan of the intensity along the vertical axis of the diffractogram. In Fig.24c a conventional TEM image (without phase plate) taken at 450 nm underfocus of the same sample area is shown. The 2.3nm spacing of coat protein arrays along the TMV axis is clearly visible in both the reconstructed phase (Fig.24a) and the conventional image (Fig.24c). Higher frequency components are equally preserved in the two images, but the addition of low frequency components, recovered exclusively in PTEM, results in significantly less distortion in the reconstructed image (Fig.24a).

The signal intensity reflected in the TMV images can be quantified using diffractograms (lower insets of Figs.24a and b). The dominance of signals in the phase rather than the amplitude is evident from a comparison of the diffraction peaks which reflect the 2.3nm spacing. Their intensity ratio is about 5:1, as would be expected for samples stained with heavy metals [46].

The completeness of the information displayed in the complex images is verified by the simulated TMV image shown in Fig.24d. This image was obtained by assuming that the aberration-free complex pair (Figs.24a and b) directly represents the object wave function and applying the same CTF as in the conventional image (Fig.24c). The simulated (Fig.24d) and the mimicked (Fig.24c) images are remarkably similar. Note that the defocus value of the mimicked image (+495 nm) is completely different from that of the original complex pair (-2200 nm).

3.2.3. Discussion.

The experimental results presented above show that complex reconstruction is applicable in practice. The reconstructed images are free from aberrations and provide the full information contained in the object wave. The availability of the recovered amplitude information about the sample can provide a more quantitative way of evaluation in the future.

Specimen damage due to electron bombardment is very important factor in high resolution biological observations. The specimen resolution decreases with the increase of the electron dose. Any loss of information during the observation increases the time and effort needed for solving the sample structure. The fact that only two photos are required for the complete information to be recovered makes complex reconstruction far superior to the widely used defocus series. However from an experimental point of view it is still less attractive. The complicated procedures related to the application of the Zernike phase plate

reduce the success rate of the photos and thus the overall effectiveness of the experiments.

Provided that most of the phase plate application problems discussed in Chapter 1 are solved complex reconstruction could become a standard in the high resolution biological observations.

CONCLUSIONS

The Zernike phase plate was successfully applied to TEM. For the first time in TEM history a cosine-type phase CTF is demonstrated. An image formation theory and optimal defocus definition for the PTEM are presented. Images of negatively stained horse spleen ferritin obtained with PTEM show remarkable contrast and clarity compared to images acquired with CTEM. Many practical problems still plaguing the phase plate application have been recognized and possible solutions are proposed.

The electrostatic charging recognized as the major problem in the phase plate application was subjected to detailed investigation. For that purpose a new experimental technique for measurement of charging of thin films under electron irradiation was developed – Differential Electron Interferometry (DEI). Combined with the solution of the inverse Laplace problem the technique provides the radial distribution of the surface charge density. Investigation of the charging performed by DEI showed that contamination residing on the surface of the film is the main source of electrostatic charging.

The originally proposed complex observation scheme was improved. The developed off-plane application scheme overcomes the problem with electrostatic charging of the phase plate. The first successful application of the complex reconstruction scheme is presented. The complex form of the object wave has been reconstructed for negatively stained samples of horse spleen ferritin and tobaco mosaic virus. The reconstructed wave is free from aberrations and represents the sample much better than the CTEM images. Provided that most of the phase plate application problems are solved complex reconstruction could become a standard in the high resolution biological observations.

ACKNOWLEDGEMENTS

REFERENCES

[1] O. Scherzer, J. Appl. Phys. 20 (1949) 20.

[2] E. J. Kirkland, Ultramicroscopy 15 (1984) 151.

[3] W. Coene, G. Janssen, M. O. de Beeck, D. Van Dyck, Phys. Rev. Lett. 69 (1992) 3743.

[4] R. Schröder, W. Hofmann, J.-F. Ménétret, J. Struct. Biol. 105 (1990) 28.

[5] F. Zernike, Physica 9 (1942) 686.

[6] K. Kanaya, H. Kawakatsu, J. Appl. Phys. 29 (1958) 1046.

[7] J. Faget, M. Fagot, J. Ferré, C. Fert, Proc. Fifth International Congress for Electron Microscopy , Academic Press, New York, 1962, A-7.

[8] H. Badde, L. Reimer, Z. Naturforsch 25a (1970) 760.

[9] F. Thon, in: U. Valdre (Ed.), Electron Microscopy in Material Sciences, Academic Press, London, 1971, p. 571.

[10] D. Parsons, H. Johnson, Appl. Opt. 11 (1972) 2840.

[11] H. M. Johnson, in: H. A. Hayat (Ed.), Principles and Techniques of Electron Microscopy, Vol. 3, Van Nostrand Reinhold Co., New York, 1973, p.153.

[12] D. Willasch, Optik 44 (1975) 17.

[13] T. Matsumoto, A. Tonomura, Ultramicroscopy 63 (1996) 5.

[14] M. Born, E. Wolf, Principles of Optics, Ed. 7, University Press, Cambridge, 1999.

[15] L. Reimer, Transmission Electron Microsocpy, Physics of Image Formation and Microanalysis, Ed. 4, Springer, New York, 1997.

[16] K. Hanszen, Z. Angew. Phys. 20 (1966) 427.

[17] K. Hanszen, in: R. Barer (Ed.), Advances in Optical and Electron Microscopy, Vol. 4, Academic press, London, 1971, p.1.

[18] V. Cosslett, Biochem. et Biophys. Acta, 2 (1948) 239.

[19] K. Danov, R. Danev, K. Nagayama, Ultramicroscopy, 87 (2001) 45

[20] W. Bigelow, in: A. Glauert (Ed.), Vacuum Methods in Electron Microscopy, Practical Methods in Electron Microscopy, Vol. 15, Portland Press, London, 1994.

[21] S. Utteridge, V. Sushin, S. Canney, M. Ford, Z. Fang, D. Oliver, M. Vos, E. Weigold, Appl. Surf. Sci. 162-163 (2000) 359.

[22] K. Nagayama, J. Phys. Soc. Jpn., 68 (1999) 811.

[23] R. Danev, K. Nagayama, J. Phys. Soc. Jpn. 70 (2001) 696.

[24] J. Cazaux, J. Appl. Phys. 59 (1986) 1418.

[25] E. Plies, in: Vol. 13 of Advances in Optical and Electron Microscopy, Eds. T. Mulvey and C. J. R. Sheppard (Academic Press, New York, 1994) p. 123.

[26] J. Cazaux, Ultramicroscopy 60 (1995) 411.

[27] G. Matteucci, G.-F. Missiroli, E. Nichelatti, A. Migliori, M. Vanzi and G. Pozzi, J. Appl. Phys. 69 (1991) 1835.

[28] B. G. Frost and T. L. Jenkins, Journal of Microscopy 187 (1997) 85.

[29] B. G. Frost, Ultramicroscopy 75 (1998) 105.

[30] B. G. Frost and E. Voelkl, Ultramicroscopy 72 (1998) 101.

[31] P. N. T. Unwin, Phil. Trans. Roy. Soc. Lond. B 261 (1971) 95.

[32] J. Rouse, in: Vol. 13 of Advances in Optical and Electron Microscopy, Eds. T. Mulvey and C. J. R. Sheppard (Academic Press, New York, 1994) p. 1.

[33] W. Krakow and B. Siegel, Optik 42 (1975) 245.

[34] M. Kuzuya, M. Hibino and S. Maruse, Ultramycroscopy 15 (1984) 233.

[35] T. Hanai, M. Hibino and S. Maruse, J. Electron Microsc. 31 (1982) 360.

[36] G. Love, V. Scott, N. Dennis, L. Laurenson, Scanning 4 (1981) 32.

[37] K. D. Danov and K. Nagayama, J. Appl. Phys (2000) – submitted.???

[38] C. Pozrikidis, Introduction to Theoretical and Computational Fluid Dynamics. (Oxford University Press, New York, 1997).

[39] K. Danov, R. Danev, K. Nagayama, "Reconstruction of the electric charge density in thin films from the contrast transfer function measurements", Ultramicroscopy (2001) in press.

[40] K. H. Müller, Optik 33 (1971) 296.

[41] H. Lichte, Ultramicroscopy 20 (1986) 293.

[42] T. Kawasaki, Q. Ru, T. Matsuda, Y. Bando, A. Tonomura, Jpn. J. Appl. Phys. 30 (1991) L1830.

[43] U. Weierstall, H. Lichte, Ultramicroscopy 65 (1996) 13.

[44] P. Schiske, Proc. 14th European Conference on Electron Microscopy, Rome, D. Bocciarelli (Ed.), Topografia Poliglotta Vaticana, Rome, 1968, Vol. 1, p. 145.

[45] K. Ishizuka, T. Tanji, A. Tonomura, T. Ohno, Y. Murayama, Ultramicroscopy 53 (1994) 361.

[46] H. Erickson, A. Klug, Phil. Trans. Roy. Soc. London B26 (1971) 105

Element	Inner potential* [V]	-π/2 thickness [nm]	
		100 kV**	300 kV**
$_4$Be	7.8	21.79	30.86
$_6$C	7.8	21.79	30.86
$_{13}$Al	12.1	14.04	19.89
$_{14}$Si	11.5	14.78	20.93
$_{29}$Cu	20.1	8.45	11.97
$_{32}$Ge	15.6	10.89	15.43
$_{47}$Ag	20.7	8.21	11.63
$_{74}$W	23.4	7.26	10.29
$_{79}$Au	21.1	8.05	11.41

*: values taken from the literature (Ref.[15] page 51)
**: acceleration voltage

Table 1 Calculated thickness for -π/2 phase shift for films made of different chemical elements.

a

b

Ideal system

Practical system

Object

Objective lens

Back-focal plane

Imaging lens

Image
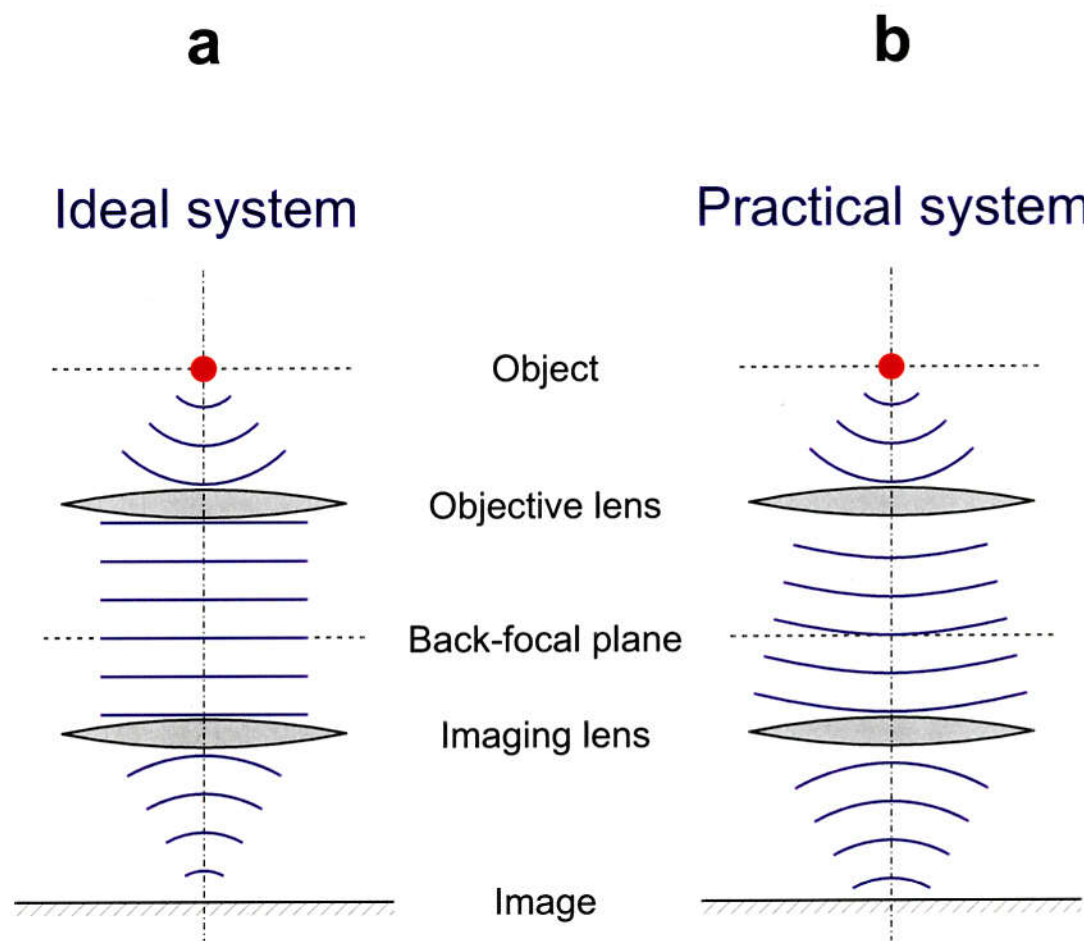
Figure 1 Illustration of ideal (a) and practical (b) optical systems. In the ideal system the spherical wave scattered from a point object at the front-focal plane of the objective lens is transferred to a plane wave at the back-focal plane. In the practical system the wave is deformed due to various imperfections in the system.

TEM image formation
CTF formalism

Object — $\psi(\vec{r})$ *object wave*

FT

Objective lens

$\Psi(\vec{k}) = FT\{\psi(\vec{r})\}$ *diffraction wave*

Back-focal plane — $\gamma(\vec{k})$ k **CTF**

$\Psi'(\vec{k}) = \Psi(\vec{k})e^{i\gamma(\vec{k})}$ *modulated diffraction wave*

Imaging lens **FT**

$\psi_i(\vec{r}) = FT\{\Psi'(\vec{k})\}$ *image wave*

$|...|^2$

Image $I(\vec{r}) = |\psi_i(\vec{r})|^2$ *image intensity*
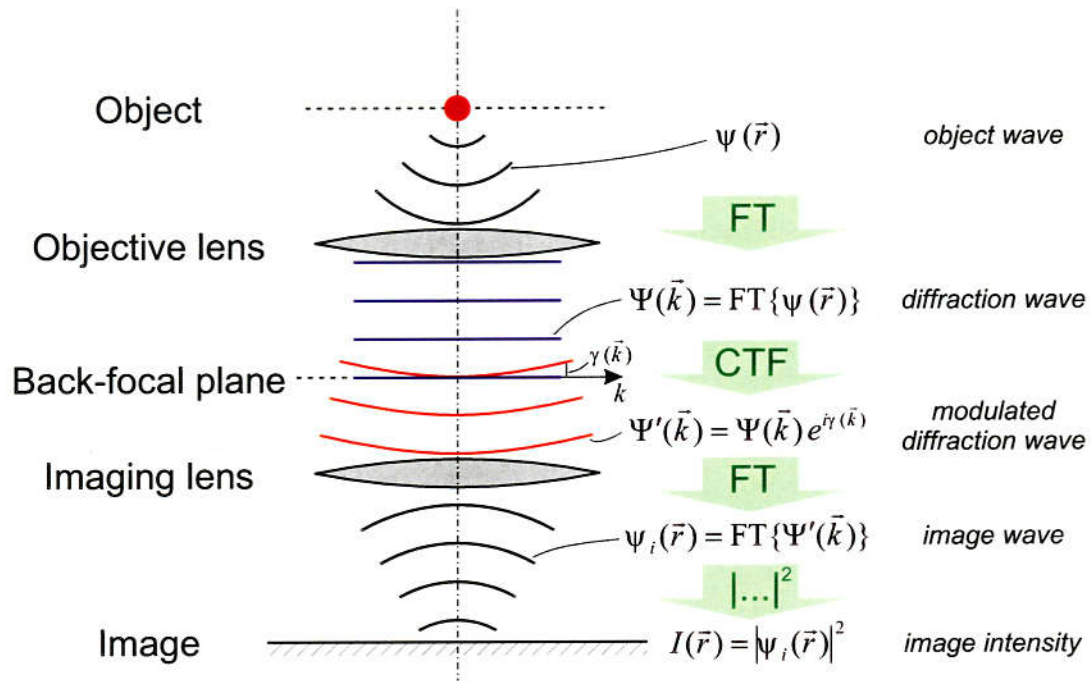
Figure 2 Illustration of the Contrast Transfer Function (CTF) formalism for description of the image formation in TEM. The Fourier transform (FT) of the object wave gives the diffraction wave. CTF modulation and another FT results in the image wave. The image intensity is equal to the squared modulus of the image wave.
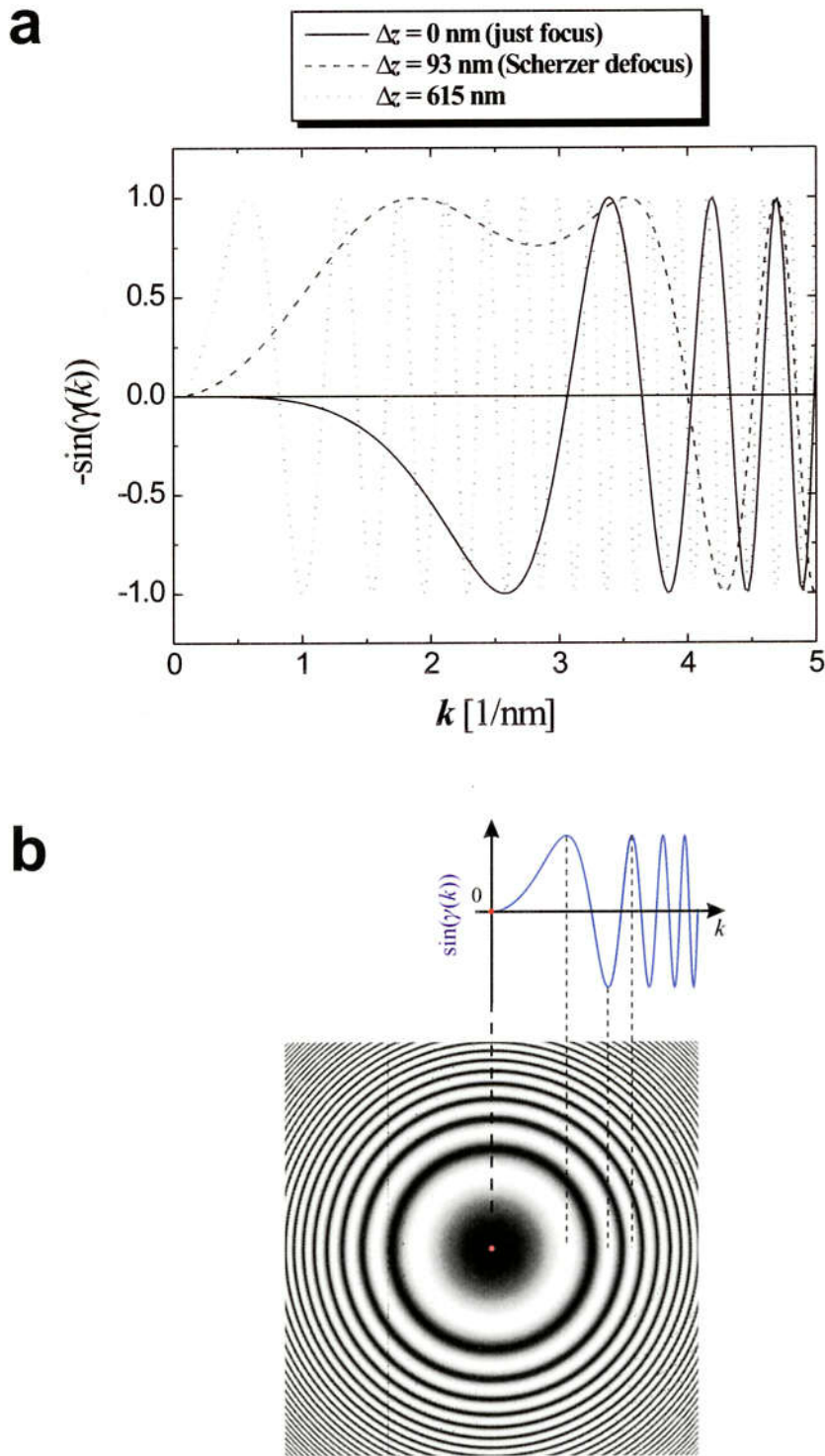
Figure 3 (a) Representative plots of the radial component of CTEM phase CTF. Acceleration voltage 300 kV, spherical aberration C_s = 3 mm. (b) Illustration of a phase CTF in the modulus of the Fourier transform of an image.

Weak-phase object

CTEM $\Delta z = 0$ nm
(just focus)
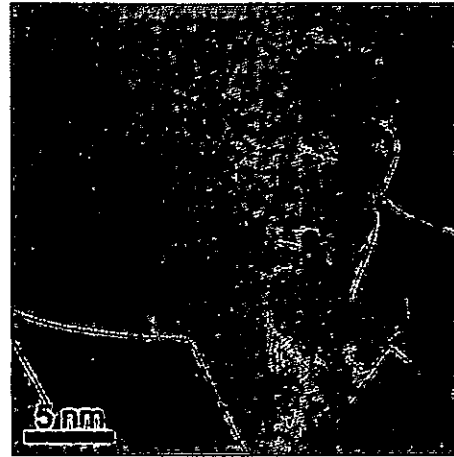
CTEM $\Delta z = 93$ nm
(Scherzer defocus)

CTEM $\Delta z = 615$ nm

Figure 4 Illustration of the compromise of contrast and direct resolution in CTEM. Simulation of images of a weak phase object at different defocus values (marked above each picture). Acceleration voltage 300 kV, spherical aberration $C_s = 3$ mm.
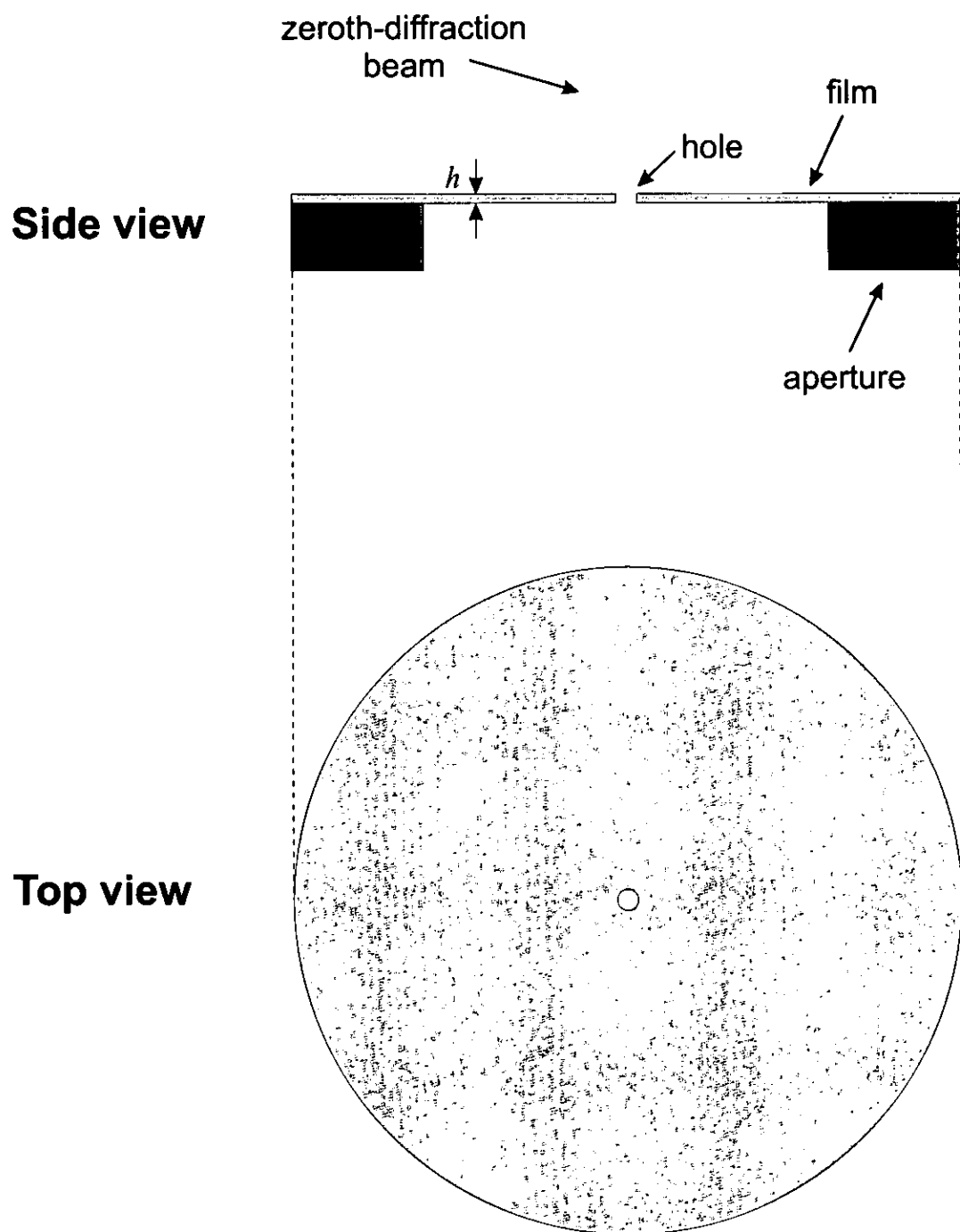
Figure 5 Schematic of the Zernike phase plate. Thin material film with thickness h is supported on an aperture. In the center of the film a hole is drilled where the zeroth-diffraction beam passes.
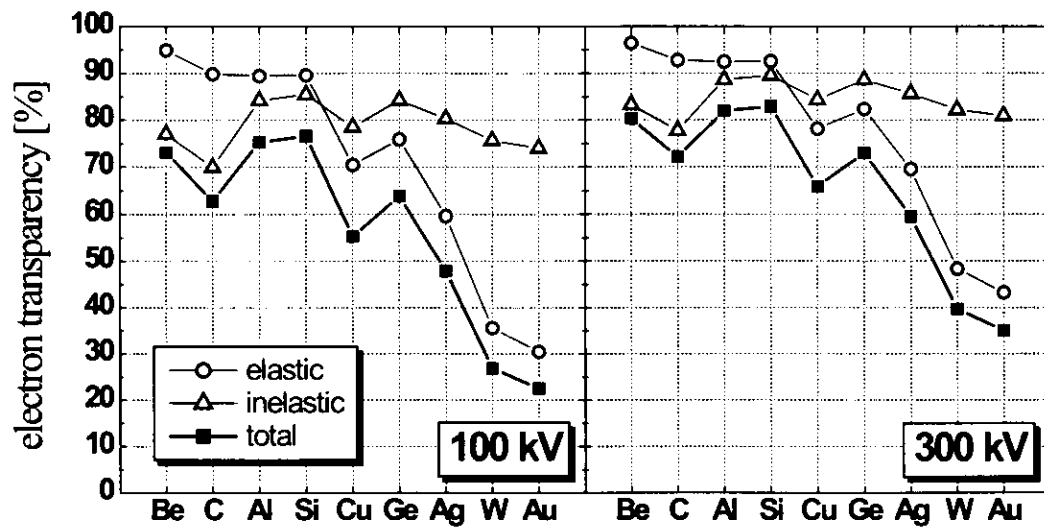
Figure 6 Elastic, inelastic and total electron transparency calculated for films with a thickness to obtain a $-\pi/2$ phase shift (from Table 1). The chemical element symbols are indicated on the horizontal axis. The graph has two sets of plots, one for 100 kV and one for 300 kV acceleration voltage.
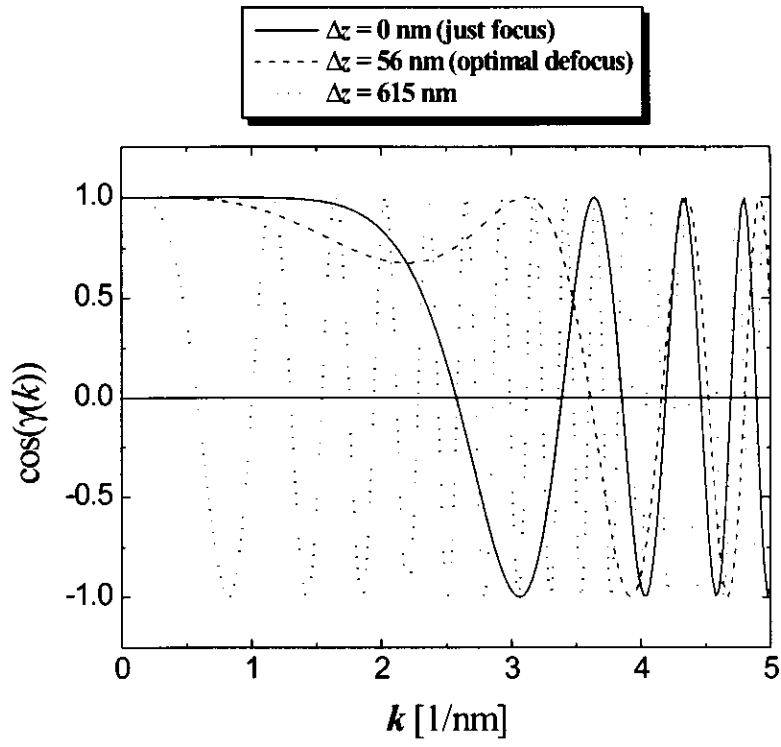
Figure 7 Representative plots of the radial component of PTEM (TEM employing a Zernike phase plate) phase CTF. Acceleration voltage 300 kV, spherical aberration $C_s = 3$ mm.

Weak-phase object

PTEM Δz = 0 nm
(just focus)

PTEM Δz = 56 nm
(Optimal defocus)

PTEM Δz = 615 nm

Figure 8 Simulation of PTEM observation. Images of a weak phase object at different defocus values (marked above each picture). Acceleration voltage 300 kV, spherical aberration C_s = 3 mm, objective focal length f = 3.5 mm, phase plate hole diameter 1μm.
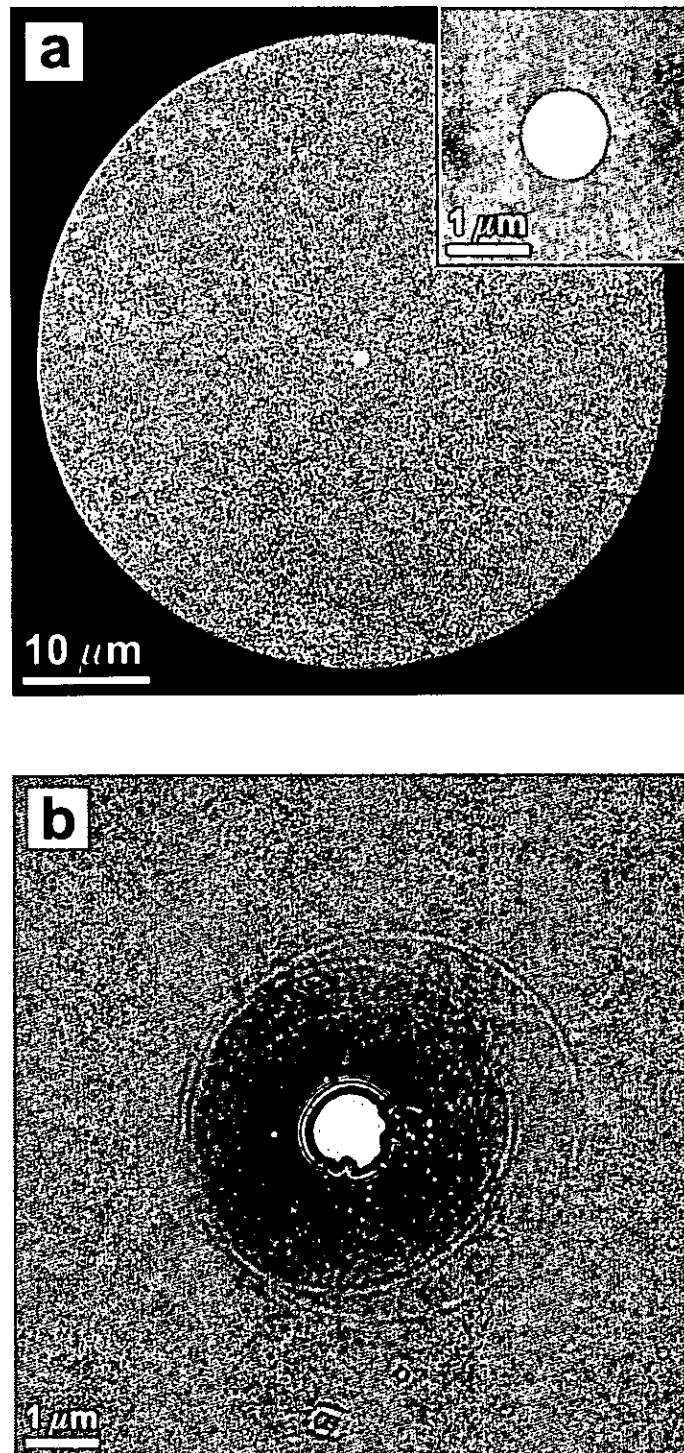
Figure 9 (a) Image of the phase plate acquired in the focused ion beam machine (JEOL JFIB-2300) used to fabricate the central hole. The inset shows a magnification of the central area. (b) TEM image of a contaminated phase plate after being used in several experiments.

a

b

1 nm^{-1}

1 nm^{-1}

c

PTEM

CTEM

|CTF|

0

0
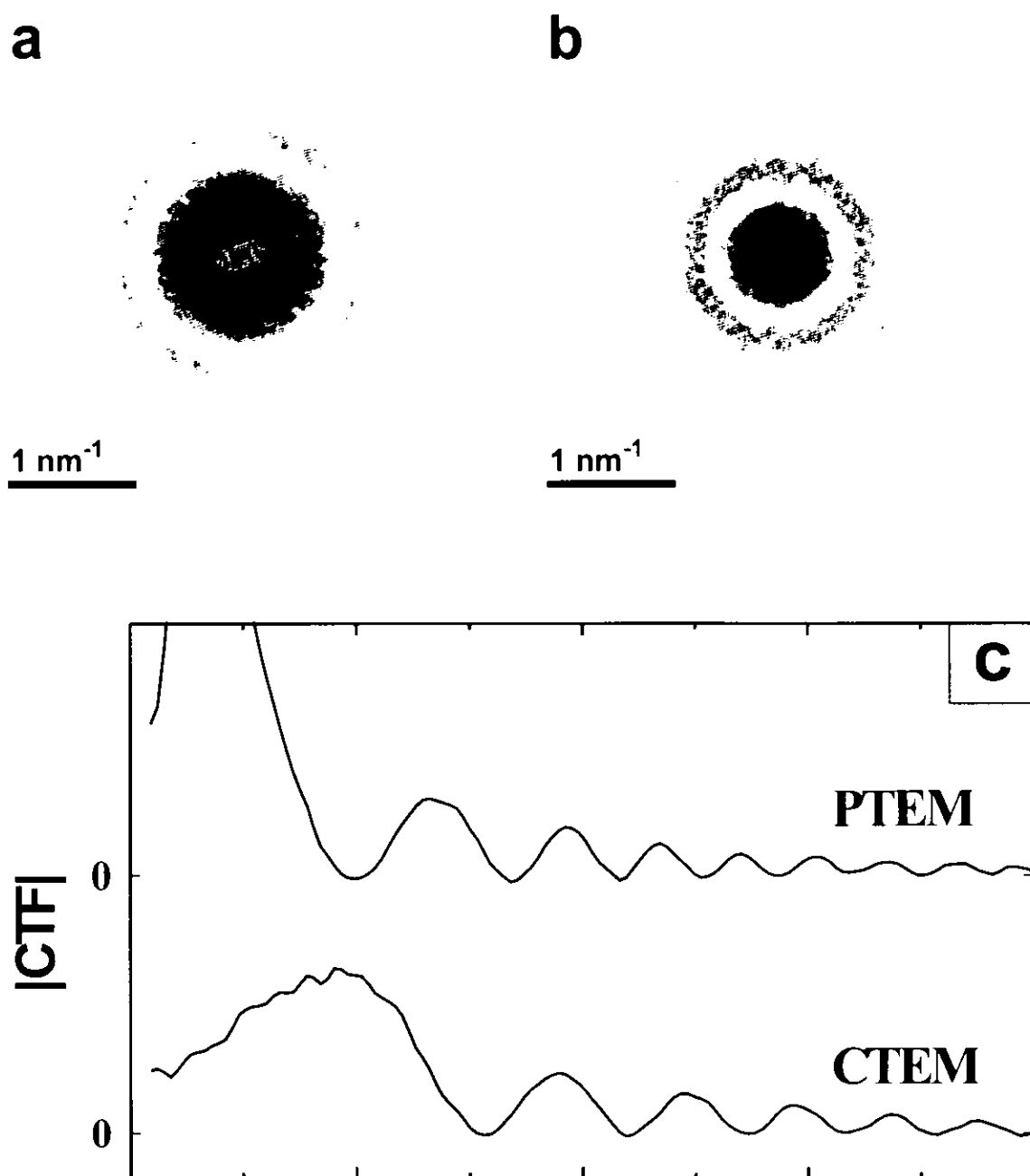
Figure 10 Diffractograms of images taken at same defocus (-830 nm, overfocus) without (a, CTEM) and with (b, PTEM) a phase plate in the back-focal plane. (c) Rotationally averaged profiles of the diffractograms. The curves are displaced vertically for clarity.
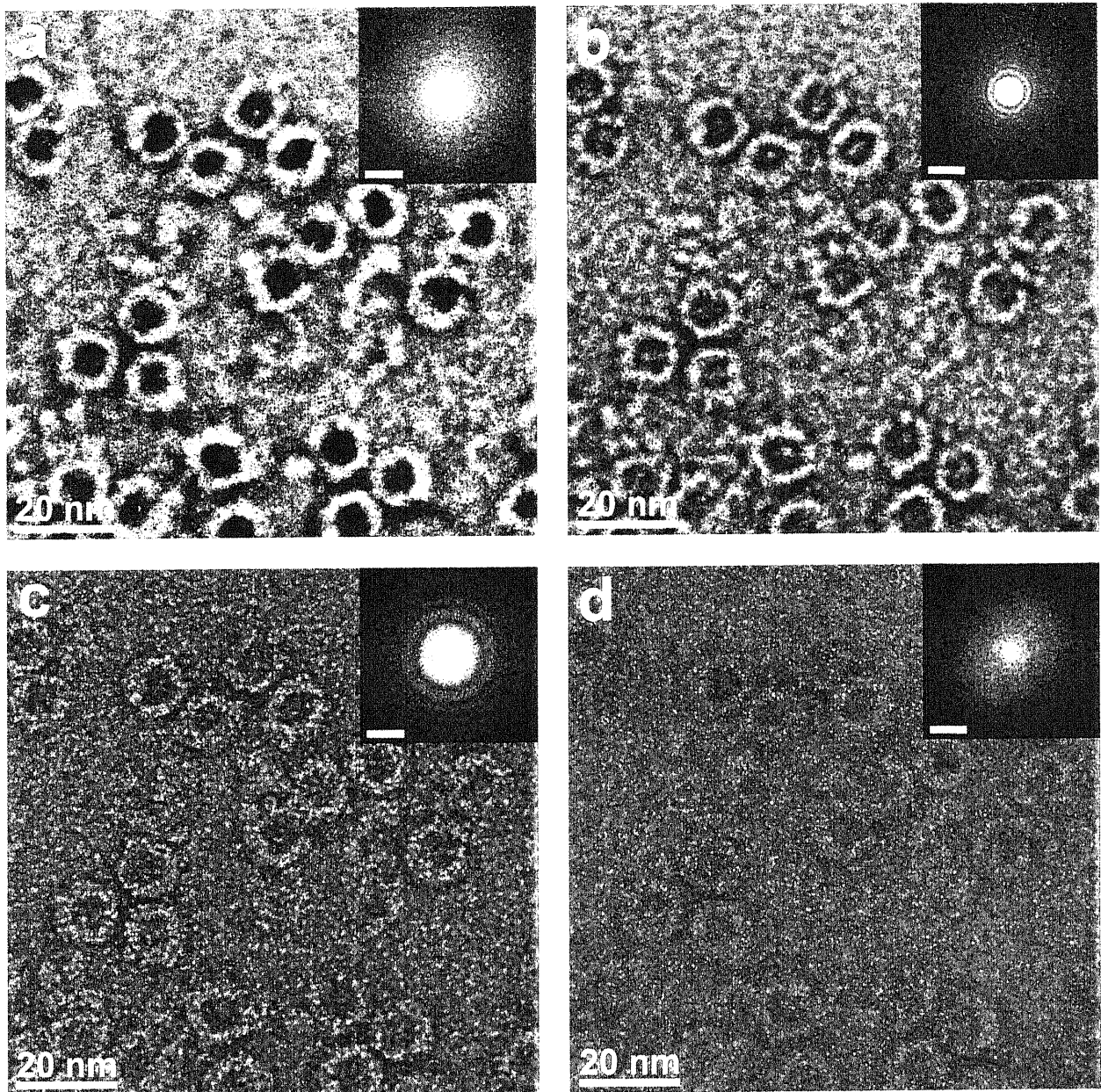
Figure 11 Images of negatively stained horse spleen ferritin. (a) phase TEM image acquired using a Zernike phase plate; (b, c and d) conventional TEM images at a defocus of 2550 nm, 540 nm and 130 nm, respectively (underfocus). The insets show the diffractogram for each image. The scale bars in the insets correspond to 1 nm^{-1}.
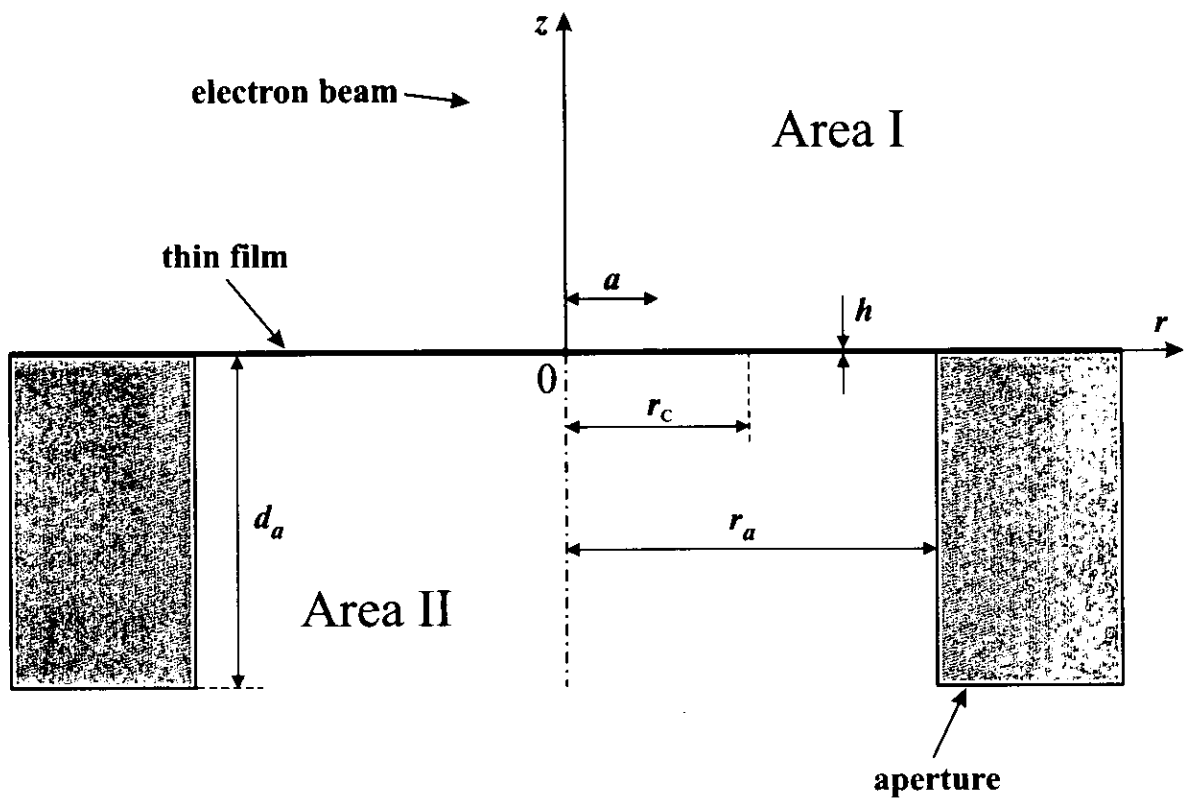
Figure 12 A sketch of the system under investigation of thin film electrostatic charging.
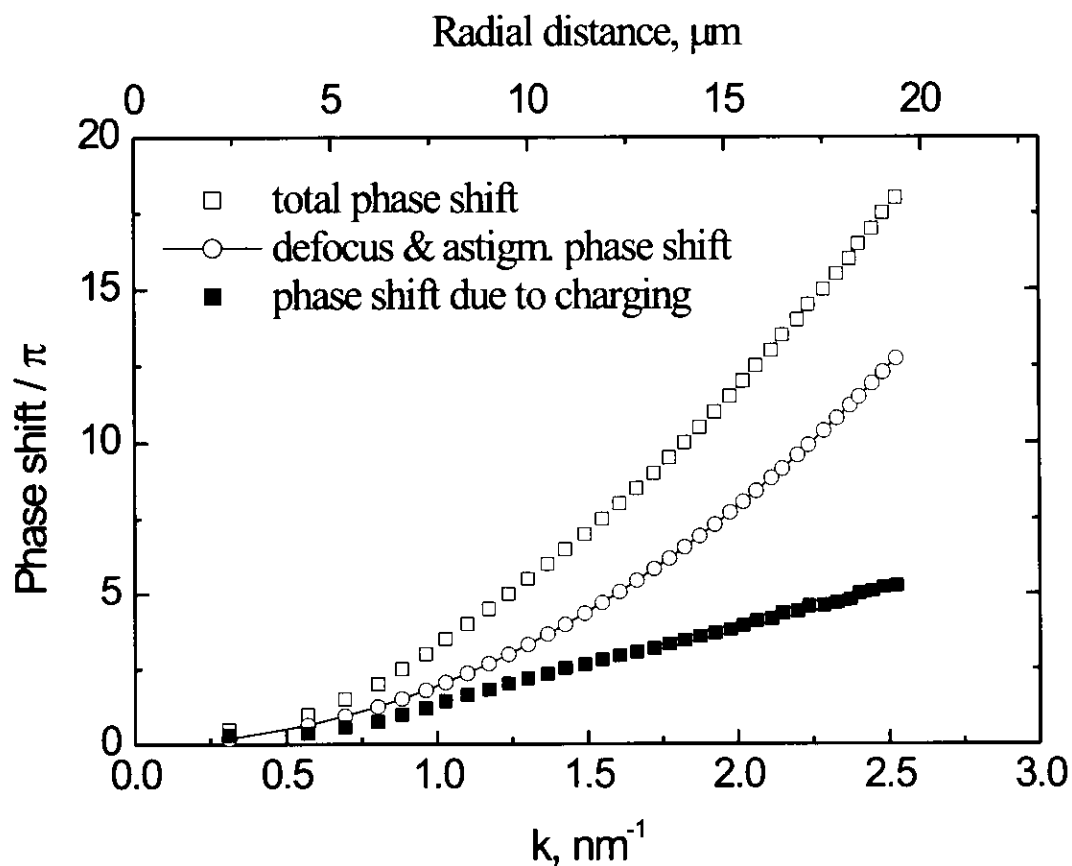
Figure 13 Illustration of the phase shift due to charging. The total phase shift is from the CTF of a photo taken with material film at the back-focal plane. The phase shift due to defocus and spherical aberration is from a photo taken without film at the back-focal plane. The difference between the two phase shifts gives the phase shift due to charging.
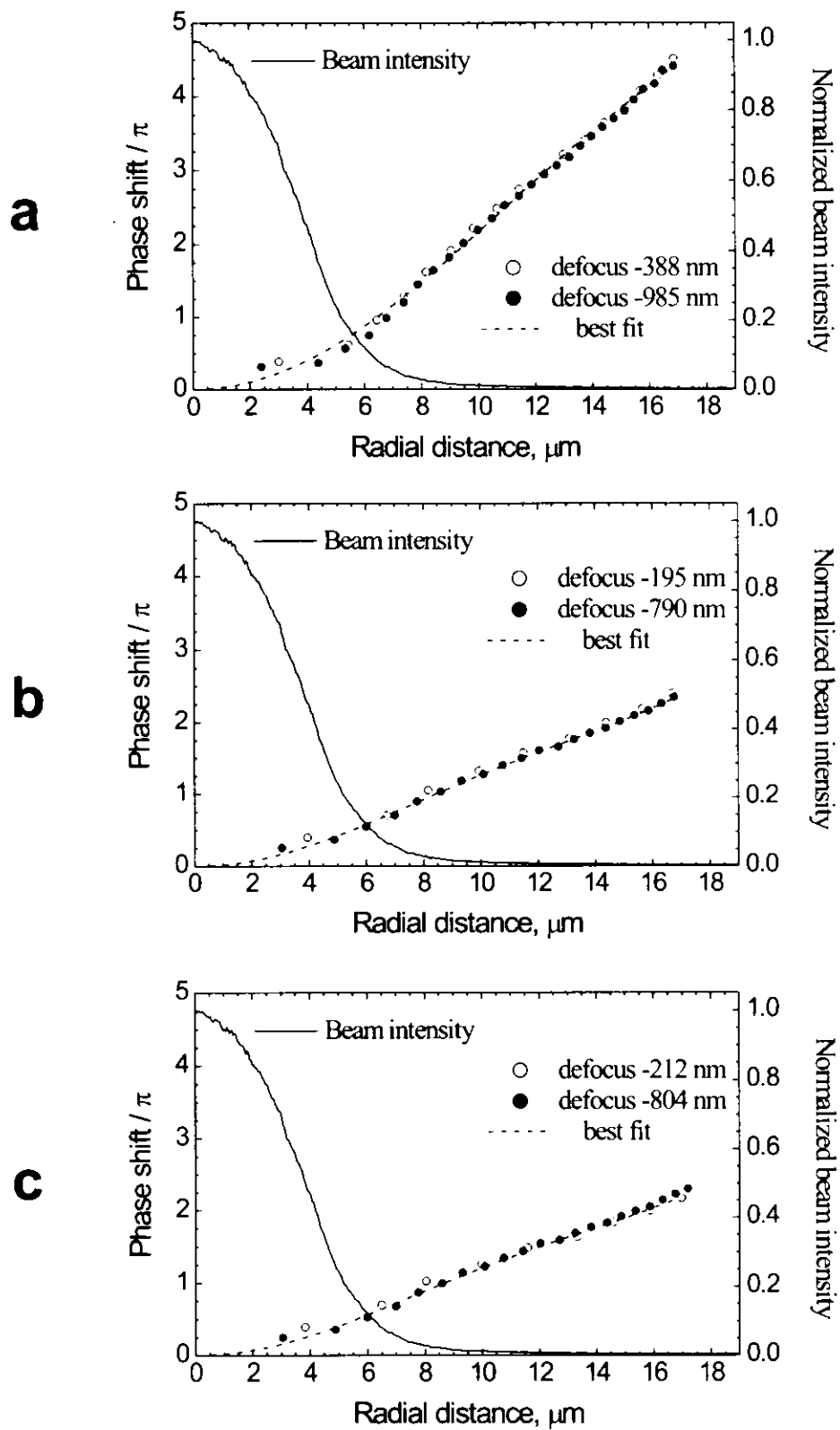
Figure 14 Experimental data for the measured phase shift due to charging after different pre-irradiation times: (a) without pre-irradiation; (b) after 30 minutes pre-irradiation; (c) after 60 minutes pre-irradiation. The solid line is the beam intensity profile. The dashed lines are the best polynomial approximations of the data.
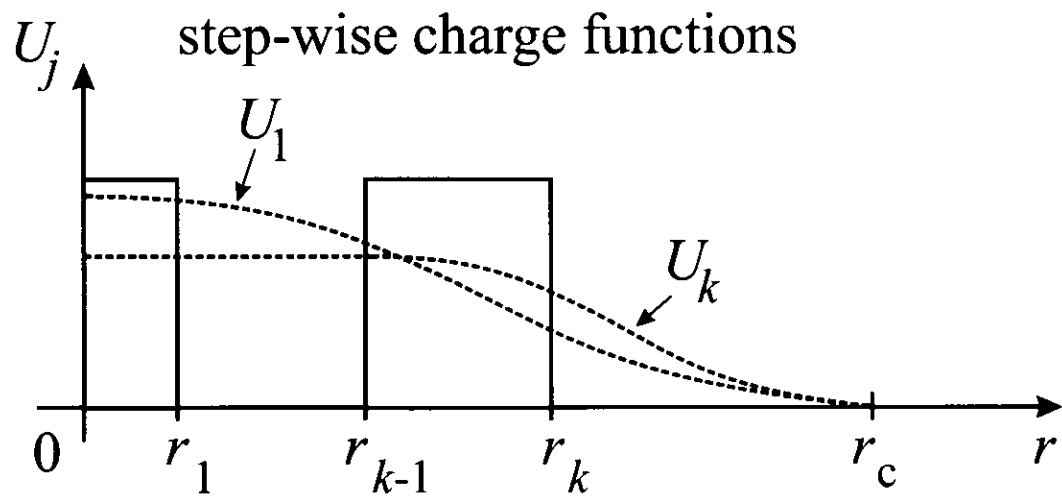
Figure 15 Illustration of the step-wise charge density approach. For each charge step function the surface potential is calculated and then used as boundary condition for the Laplace problem.
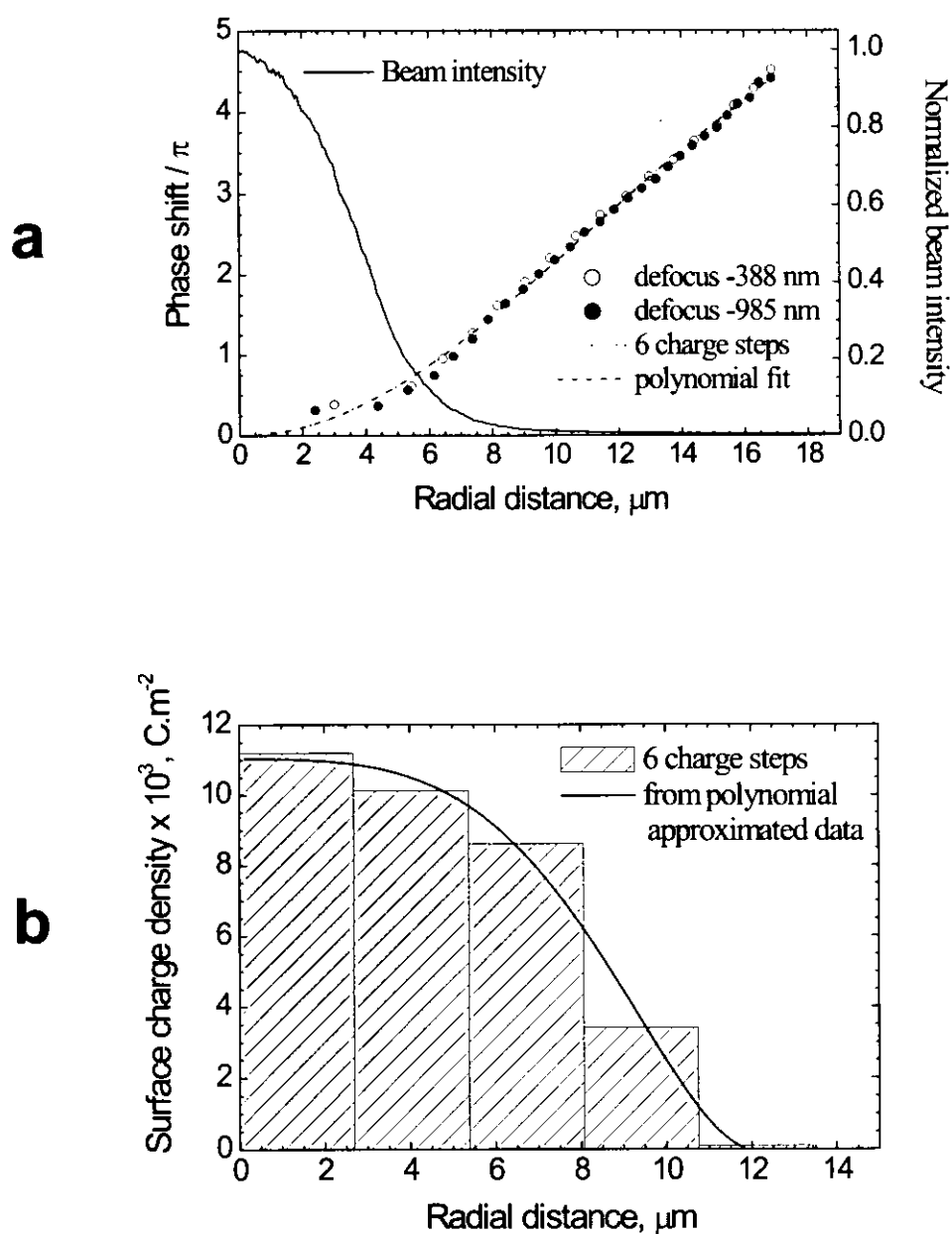
Figure 16 Comparison between the two approaches: fitting of the original experimental data with few charge stapes and fitting of polynomial approximated experimental data with a lot of charge steps. (a) The result of the six-steps calculation for the charging phase shift coincides with the polynomial approximation curve. (b) Radial charge density distributions. Both results are practically the same with the polynomial approximation method providing much smoother result (more points).
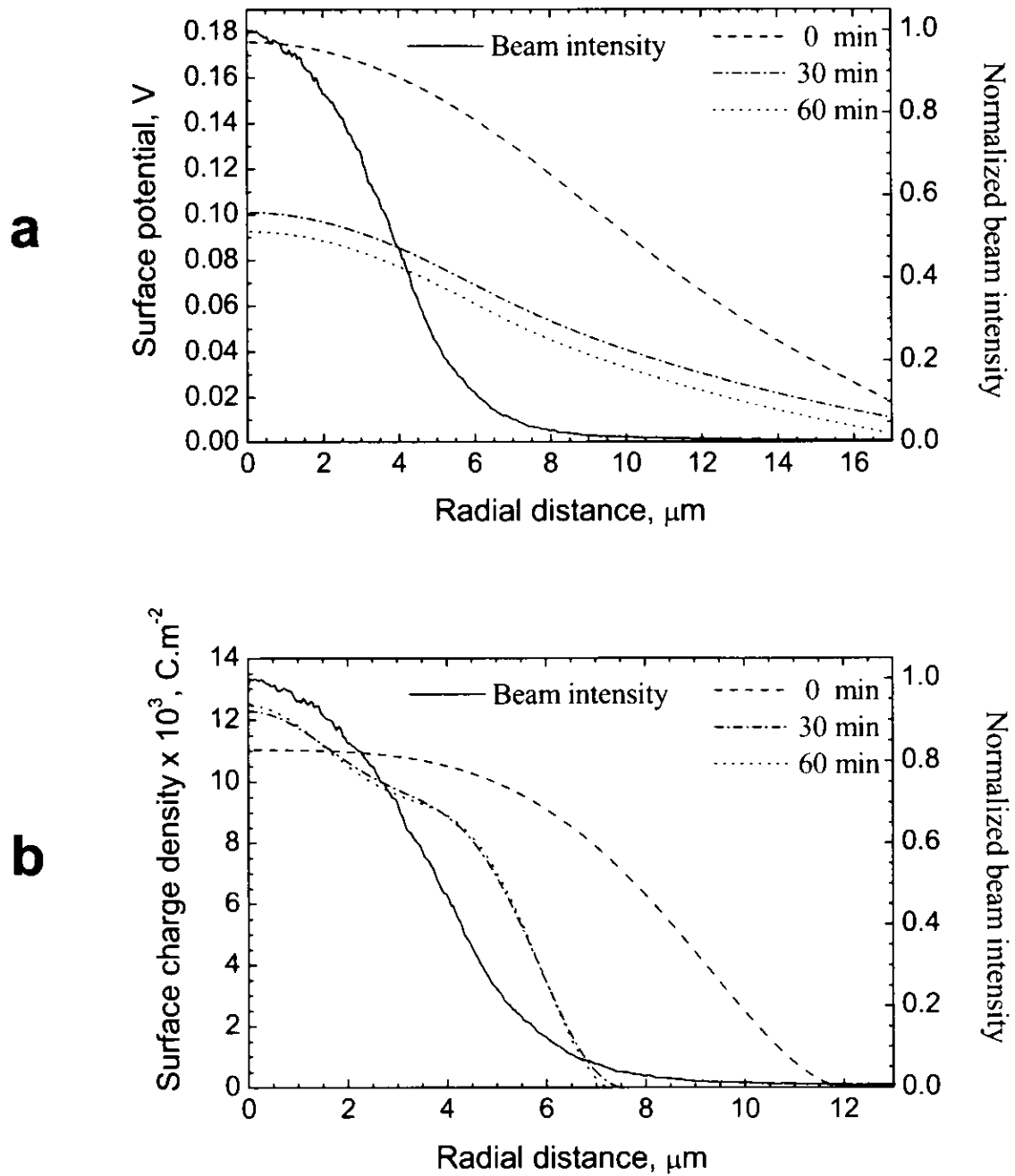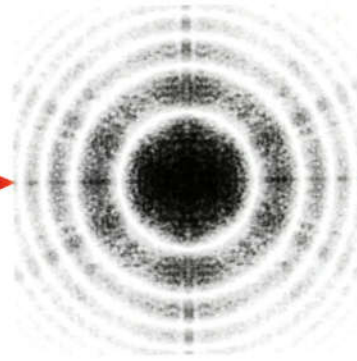
Figure 17 Results for the reconstructed surface potential (a) and charge density (b) distributions. In each plot the result for the three measurements (without pre-illumination, after 30 minutes pre-illumination and after 60 minutes pre-illuminatin) together with the electron beam intensity profile are plotted.
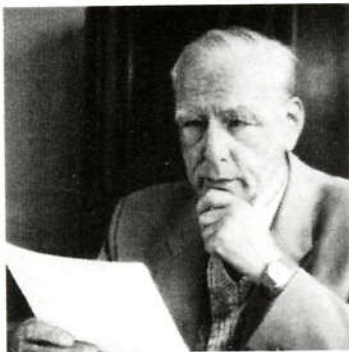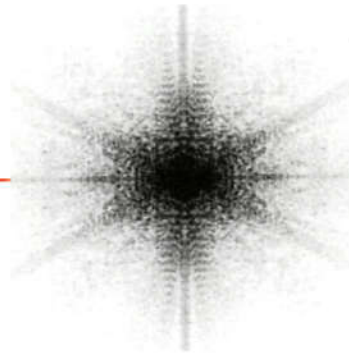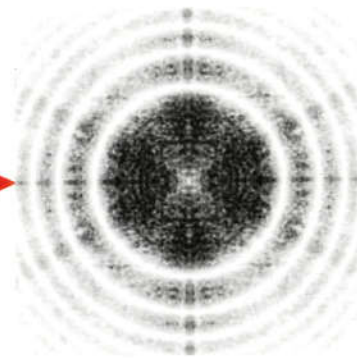
phase TEM

weak phase object

conventional TEM

FT

FT

FT

x**1**

$\exp[-i\gamma(\mathbf{k})]$
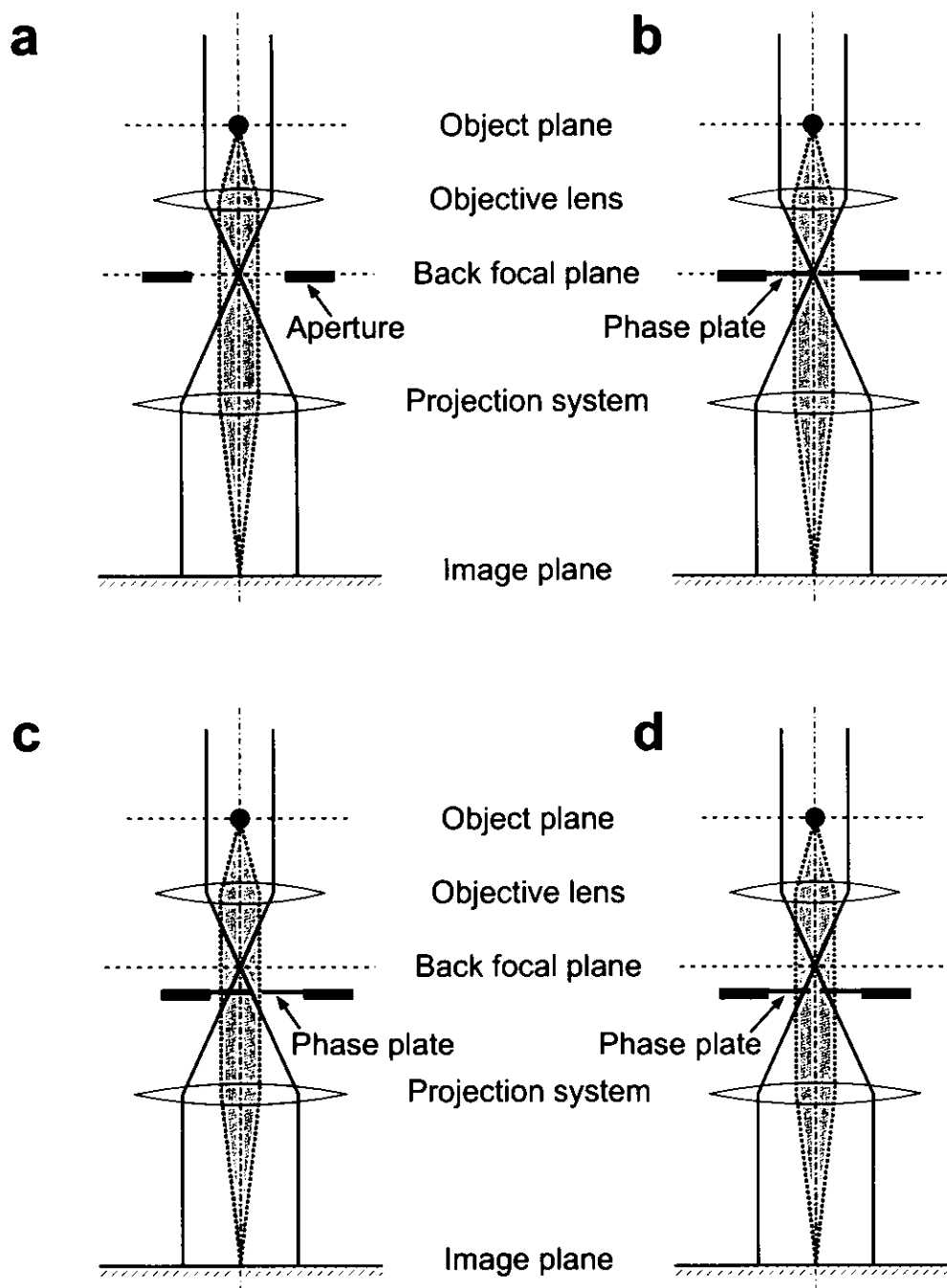
inverse
filter

x*i*
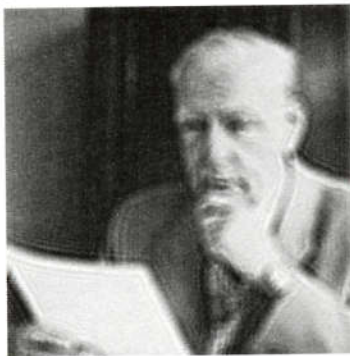
Figure 18 Illustration of the complex reconstruction scheme for observation of the complex form of the object wave. Two images are taken from the sample at identical defocus - one without (conventional TEM) and one with (phase TEM) Zernike phase plate. Complex summation and CTF inverse filtering gives the modulation-free object wave.

a

	Object plane
	Objective lens
	Back focal plane
Aperture	
	Projection system
	Image plane

b

	Object plane
	Objective lens
	Back focal plane
Phase plate	
	Projection system
	Image plane

c

	Object plane
	Objective lens
	Back focal plane
Phase plate	
	Projection system
	Image plane

d

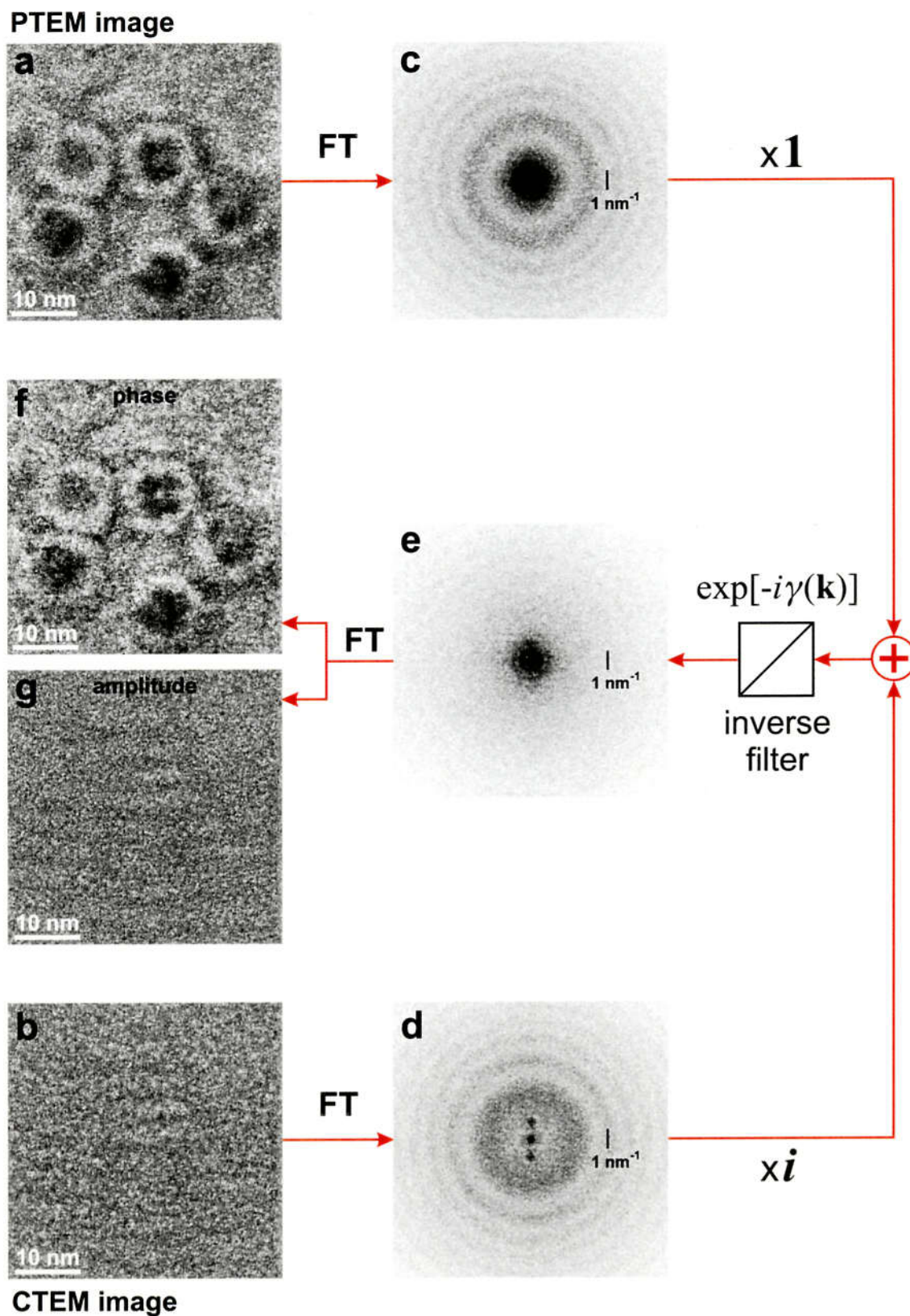|	
	Object plane
	Objective lens
	Back focal plane
Phase plate	
	Projection system
	Image plane

<u>**Figure 19**</u> Application schemes for complex reconstruction: (a,b) on-plane scheme; (c,d) off-plane scheme. The on-plane scheme uses one image without phase plate and one image with phase plate at the diffraction plane. The off-plane scheme uses two images taken with the phase plate positioned off (below or above) the diffraction plane. Between the images the phase plate is shifted (in horizontal direction) relative to the optical axis.
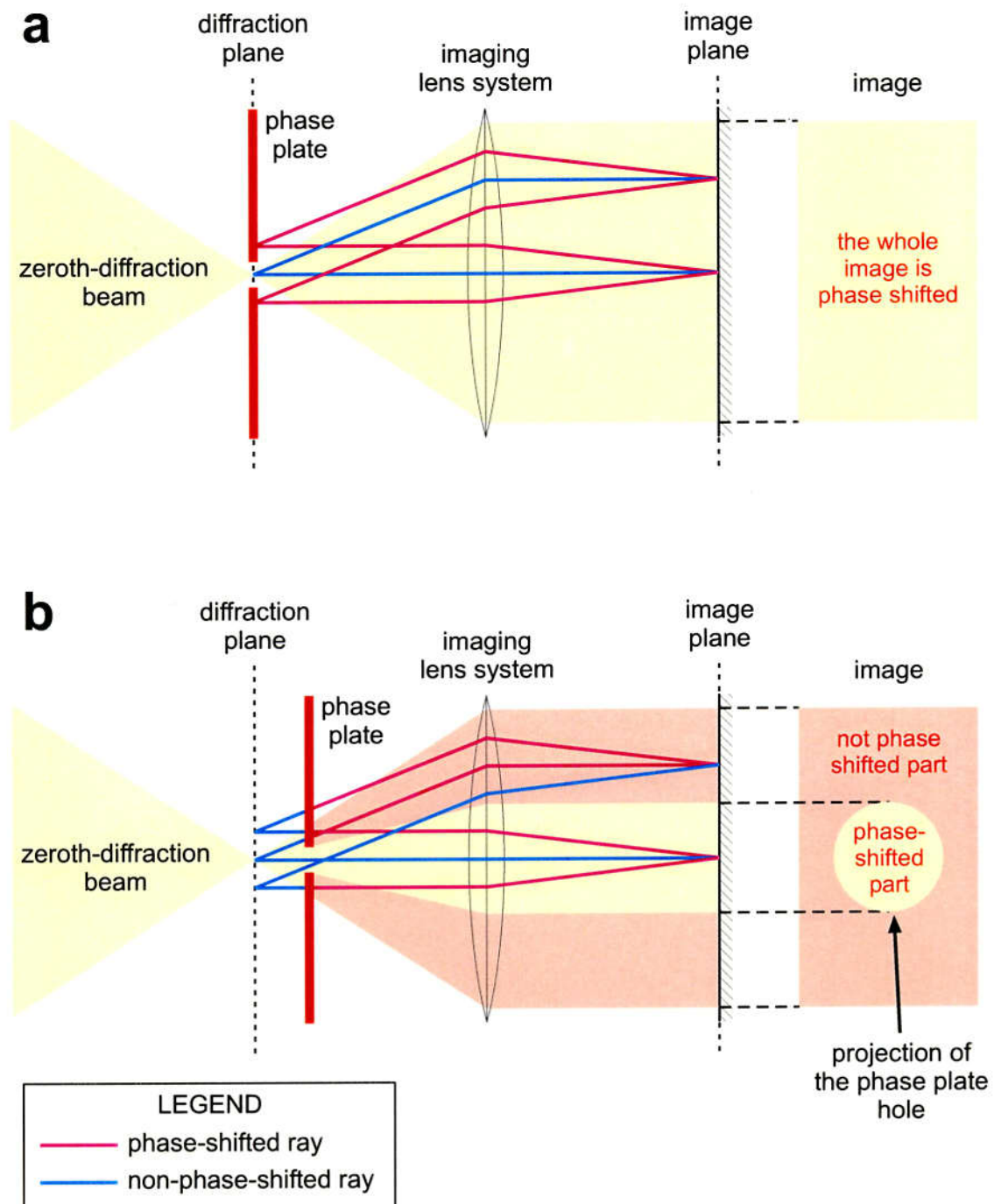
Figure 20 Geometrical optics illustration of the on-plane and off-plane application schemes. In the on-plane scheme the whole image is phase shifted (shows PTEM-like CTF). In the off-plane scheme the hole in the phase plate is projected on the image. Inside the projection the image is phase shifted (shows PTEM-like CTF). Outside the projection area the image is not phase shifted (shows CTEM-like CTF).
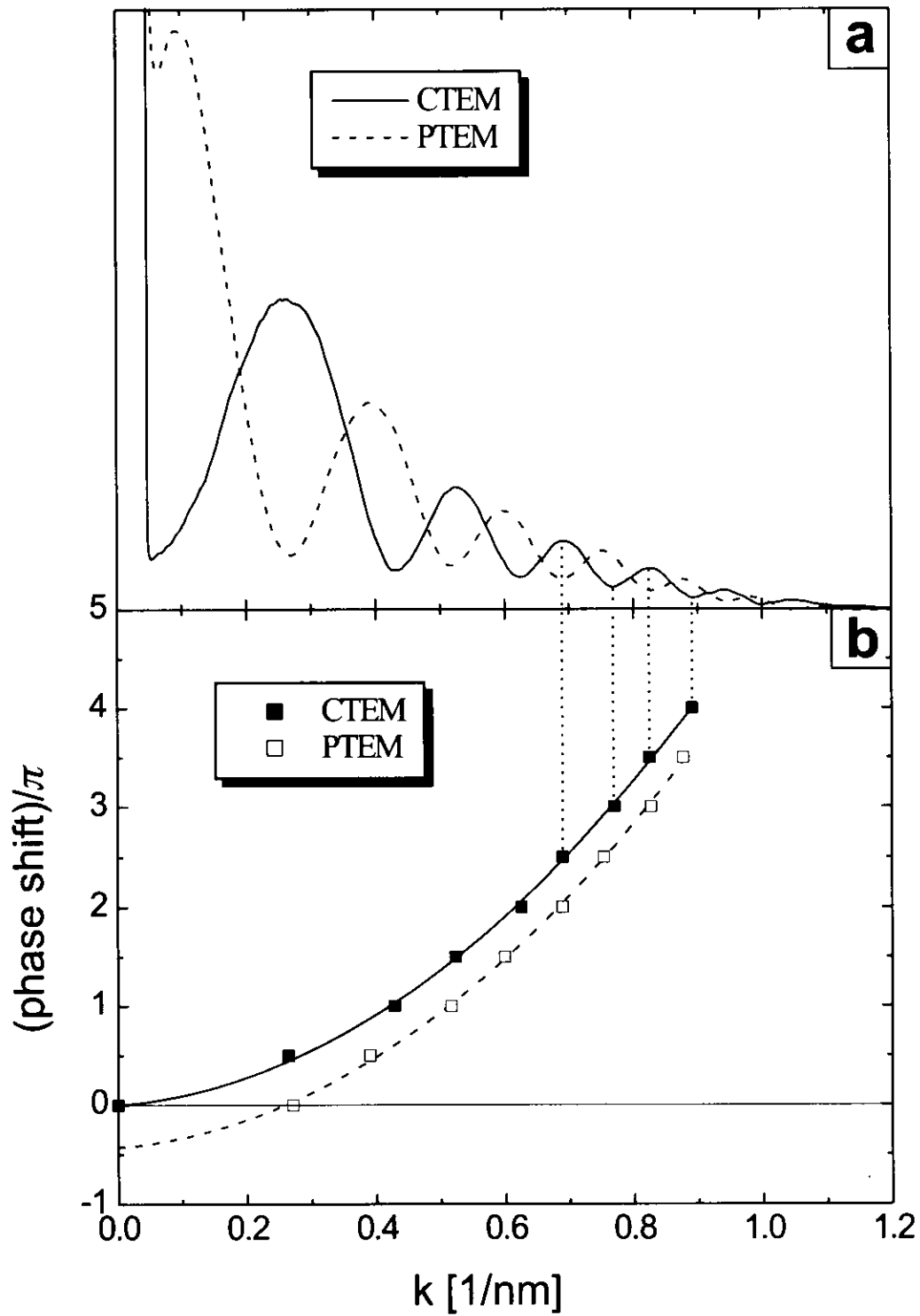
Figure 21 Illustration of the phase shift measurement technique. From the CTF profiles (a) the extrema positions are fitted giving the CTF phases (b) (illustrated for several extrema by dotted lines). The vertical difference between the CTEM and PTEM curves in (b) is the phase plate phase shift.

PTEM image

a

10 nm

FT

c

|
1 nm⁻¹

x**1**

f   phase

10 nm

g   amplitude

10 nm

FT

e

|
1 nm⁻¹

$\exp[-i\gamma(\mathbf{k})]$

inverse
filter

⊕

b

10 nm

FT

d

|
1 nm⁻¹

x***i***

CTEM image

Figure 22 Complex reconstruction of negatively stained horse spleen ferritin observed at 400 kV acceleration voltage. The PTEM and CTEM images were taken at -765 nm overfocus.

CTEM image   PTEM image
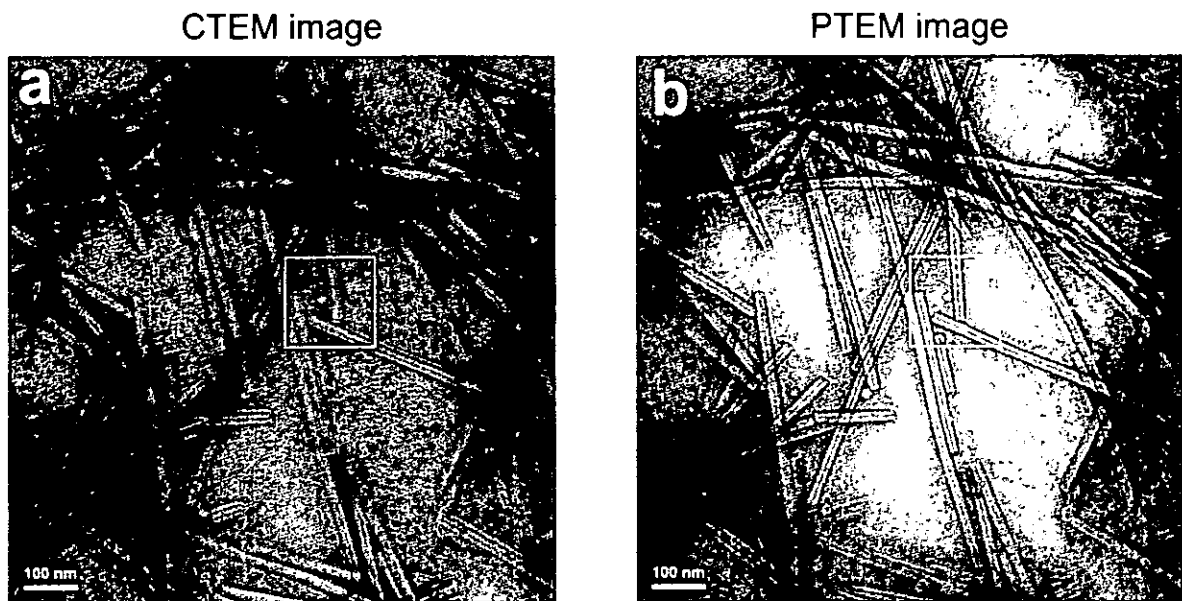
Figure 23 Complex pair of images taken from negatively stained tobacco mosaic virus at 100 kV acceleration voltage and -2200 nm overfocus. In (b) the projection of the phase plate hole is seen. The squares show the areas subjected to complex reconstruction (see Fig.24).
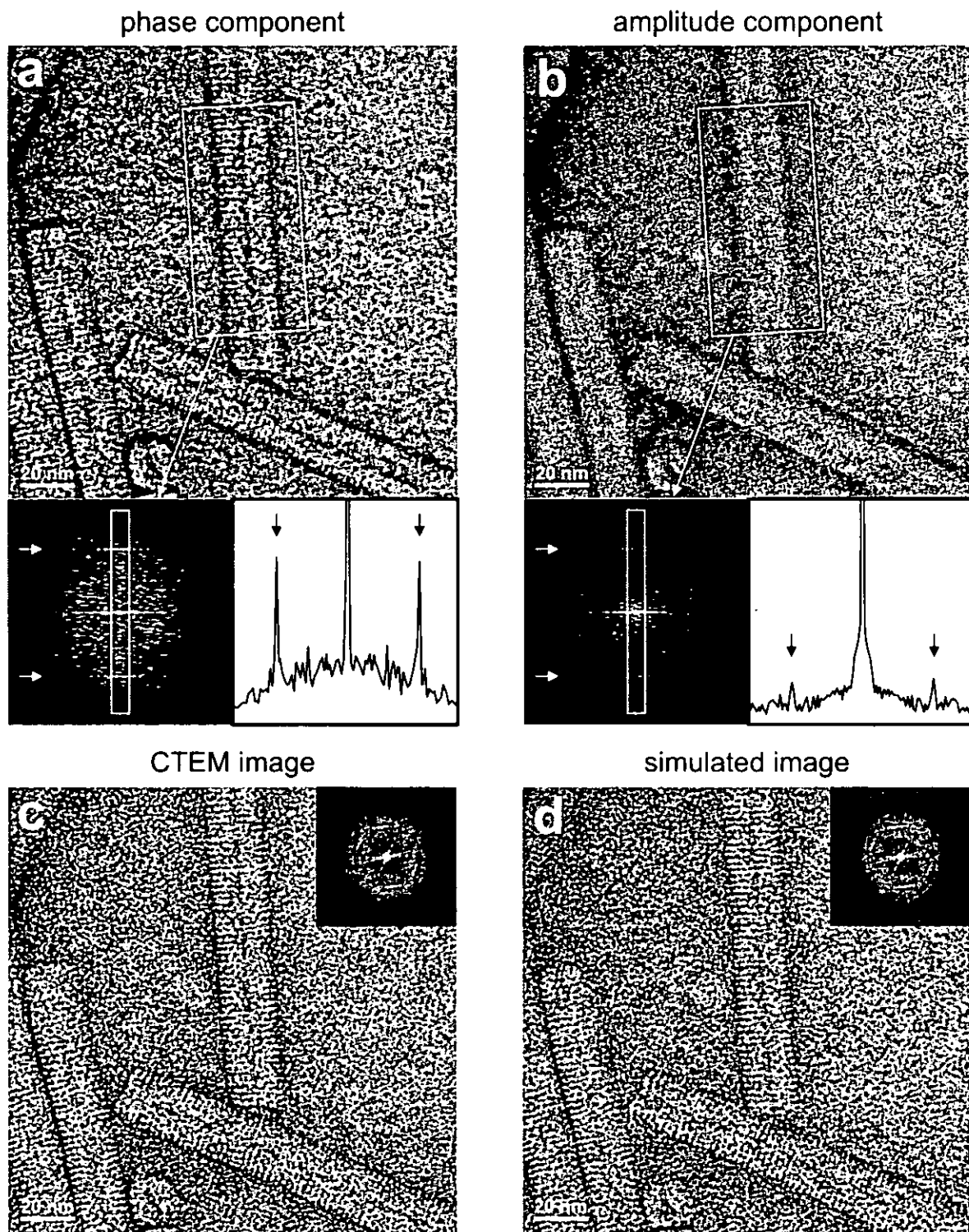
Figure 24 Reconstructed phase (a) and amplitude (b) parts from the complex pair shown in Fig.23; (c) CTEM image taken at 450 nm underfocus; (d) simulated image generated from the reconstructed complex wave (a,b) with a CTF having the same defocus as (c) (450 nm underfocus).